Received: 17 November 2018 | Revised: 16 April 2019 | Accepted: 27 May 2019

DOI: 10.1002/ddr.21557

DDR WILEY

RESEARCH ARTICLE

Novel analogs of sulfasalazine as system x_c^- antiporter inhibitors: Insights from the molecular modeling studies

Dhavalkumar Patel[1] | Prashant S. Kharkar[1] | Neha S. Gandhi[2] | Ekjot Kaur[3] | Shilpee Dutt[3] | Mukesh Nandave[1,4]

[1]Shobhaben Pratapbhai Patel School of Pharmacy and Technology Management, SVKM's NMIMS (Deemed to be University), Vile Parle (West), Mumbai, Maharashtra, India

[2]School of Mathematical Sciences and Institute for Health and Biomedical Innovation, Queensland University of Technology, Gardens Point Campus, Brisbane, Queensland, Australia

[3]Shilpee Dutt Laboratory, Advanced Centre for Treatment, Research and Education in Cancer (ACTREC), Tata Memorial Centre, Navi Mumbai, Maharashtra, India

[4]Department of Pharmacology, Delhi Pharmaceutical Sciences and Research University, New Delhi, India

Correspondence
Mukesh Nandave, Department of Pharmacology, Delhi Pharmaceutical Sciences and Research University, New Delhi, India.
Email: mukeshnandave@gmail.com

Funding information
Department of Biotechnology , Ministry of Science and Technology, Grant/Award Number: BT/PR4605/MED/30/719/2012

Abstract

System x_c^- (Sx_c^-), a cystine-glutamate antiporter, is established as an interesting target for the treatment of several pathologies including epileptic seizures, glioma, neurodegenerative diseases, and multiple sclerosis. Erastin, sorafenib, and sulfasalazine (SSZ) are a few of the established inhibitors of Sx_c^-. However, its pharmacological inhibition with novel and potent agents is still very much required due to potential issues, for example, potency, bioavailability, and blood–brain barrier (BBB) permeability, with the current lead molecules such as SSZ. Therefore, in this study, we report the synthesis and structure–activity relationships (SAR) of SSZ derivatives along with molecular docking and dynamics simulations using the developed homology model of xCT chain of Sx_c^- antiporter. The generated homology model attempted to address the limitations of previously reported comparative protein models, thereby increasing the confidence in the computational modeling studies. The main objective of the present study was to derive a suitable lead structure from SSZ eliminating its potential issues for the treatment of glioblastoma multiforme (GBM), a deadly and malignant grade IV astrocytoma. The designed compounds with favorable Sx_c^- inhibitory activity following in vitro Sx_c^- inhibition studies, showed moderately potent cytotoxicity in patient-derived human glioblastoma cells, thereby generating potential interest in these compounds. The xCT-ligand model can be further optimized in search of potent lead molecules for novel drug discovery and development studies.

KEYWORDS
cystine-glutamate antiporter, erastin, GBM, glioblastoma multiforme, sorafenib, sulfasalazine, system x_c^-

1 | INTRODUCTION

Cancer is a generic term used to describe numerous types of malignancies of the body. Despite the time and efforts worth countless dollars, cancer remains undefeated. The overall survival rate has improved by only 3.4 months in 2013 compared to the treatments available in 2003 (Salas-Vega, Iliopoulos, & Mossialos, 2017). Newer targets and treatment modalities have been and are being explored to conquer cancer (Cassetta & Pollard, 2018; Kharkar, 2017; Shah & Kharkar, 2018). In order to survive, the cancer cells have to combat oxidative stress produced as a result of aerobic metabolism (Sosa et al., 2013). In this context, cancer cells adapt by a mechanism involving manipulation of intracellular signaling through aberrant gene expression and thus maintain intracellular redox status (Balendiran, Dabur, & Fraser, 2004). To neutralize the higher concentration of reactive oxygen species (ROS) produced by the aerobic metabolism,

the cancer cells may synthesize a key antioxidant, glutathione (GSH), thereby maintaining DNA synthesis, growth, and multidrug/radiation resistance (Balendiran et al., 2004). The continuous supply of cystine is mandatory for the production of adequate levels of GSH in tumor cells (Habib, Linher-Melville, Lin, & Singh, 2015). Many studies have reported that a variety of cancer cell types like glial (Sontheimer, 2008), head and neck (Chintala et al., 2010), lung (Guan et al., 2009), breast (Balendiran et al., 2004), gastrointestinal (Ishimoto et al., 2011), pancreatic (Lo, Ling, Wang, & Gout, 2008), ovarian (Okuno et al., 2003), colon (Verrey et al., 2004), and many others maintain the intracellular redox balance by importing one molecule of cystine (which gets converted to cysteine intracellularly) with the simultaneous release of one molecule of glutamate (Figure 1).

The equimolar exchange of cystine and glutamate is mediated by system x_c^- (Sx_c^-) antiporter present in the cell membrane (Balendiran et al., 2004; Chintala et al., 2010; Guan et al., 2009; Habib et al., 2015; Ishimoto et al., 2011; Lo et al., 2008; Okuno et al., 2003; Sontheimer, 2008). Overexpression of Sx_c^- was found to be associated with increased GSH synthesis in cancer cells in vitro, ultimately compensating the antioxidant requirement of cancer cells and helping in their survival. Sx_c^-, basically a hetero(di)meric amino acid transporter (HAT), consists of two subunits, xCT and 4F2hc. The xCT subunit is known to perform the antiporter activity while 4F2hc subunit is involved in trafficking of xCT (Verrey et al., 2004; Wagner, Lang, & Bröer, 2001). Inhibitors of Sx_c^- antiporter are likely to throw cancer cells off-balance in their redox environment, thereby killing them due to excessive ROS production. Additionally, these inhibitors are also useful in several other therapeutic areas such as glutamate-induced excitotoxicity, and epileptogenesis.

In a recent review, Patel, Kharkar, and Nandave (2015) have extensively reviewed emerging roles of Sx_c^- antiporter and its inhibitors in variety of CNS disorders such as Alzheimer's disease, psychosis, drug addiction, depressive disorders, multiple sclerosis, hypoglycemic neuronal cell death, glioma, and excitotoxicity. Over the

(a)

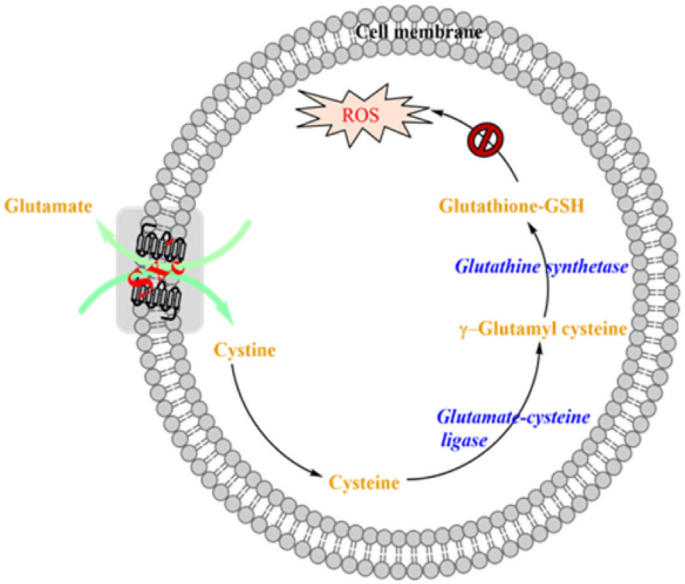

(b)

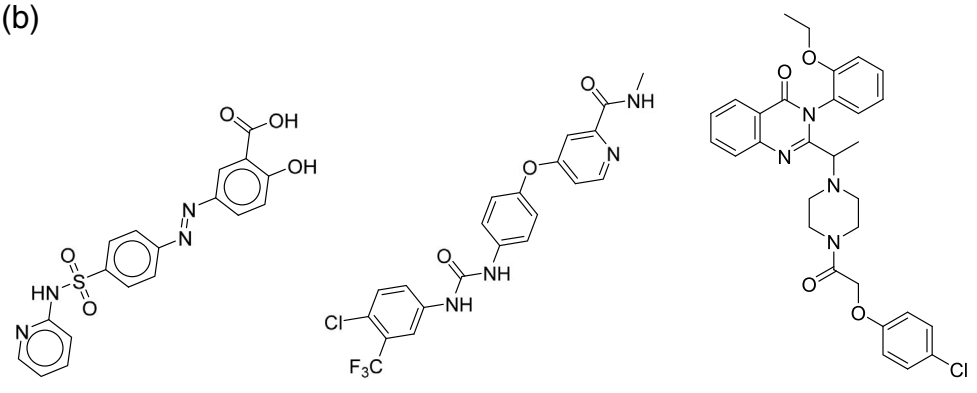

1

IC_{50} = 30 μM (U87 MG)

2

EC_{50} = 18 μM (HT1080)

3

EC_{50} = 0.2 μM (HT1080)

FIGURE 1 (a) Glutathione synthesis through intracellular movement of cystine by Sx_c^- in cancer cells to neutralize ROS; (b) molecular structures of well-known Sx_c^- inhibitor drugs along with their cellular potency data. ROS, reactive oxygen species

years, Sx_c^- antiporter always intrigued researchers for its involvement in many pathies outlined previously. In their recent work, McCormick et al. (2019) assessed the tumor redox status with the help of positron emission tomography (PET) imaging of the antiporter activity using radiotracer (*S*)-4-(3-[^{18}F]fluoropropyl)-L-glutamic acid ([^{18}F]FSPG). The authors have clearly demonstrated reduced retention of the radiotracer with increased levels of oxidative stress. In summary, the authors proposed the utility of [^{18}F]FSPG PET as an early redox indicator of tumor response following treatment. Working on the similar lines, Čolović et al. (2018) synthesized and evaluated ^{18}F-labeled boramino acid analog of aminosuberic acid for PET imaging of the antiporter. The PC3 tumor xenografts in mice were visualized using the radiotracer because the tumor cells could take it up via Sx_c^- antiporter. Both these studies unequivocally supported the importance of Sx_c^- in tumor imaging in particular. In an interesting study, Miladinovic, Ungard, Linher-Melville, Popovic, and Singh (2018) demonstrated the functional effect of the actions of neurotrophin nerve growth factor on its cognate receptor tyrosine kinase TrkA on xCT, culminating in reduced cancer-induced bone pain. The TrkA inhibitor AG879 inhibited functional system x_c^- activity. The study emphasized the importance of Sx_c^--mediated TrkA activation as a means of therapeutic intervention in cancer-related pain management.

Two FDA-approved drugs, sulfasalazine (SSZ) (**1**, Figure 1) and sorafenib (**2**, Figure 1) are few of the potent inhibitors of Sx_c^-. Additionally, erastin (**3**, Figure 1) was shown to have the highest potency among all the Sx_c^- inhibitors investigated till date (Dixon et al., 2014). Sorafenib, a conventional molecularly targeted anticancer drug, is associated with a lot of adverse effects (Dahlmanns et al., 2017; Granito et al., 2016), while erastin lacks promising in vivo anticancer data. In a recent study, Sato et al. (2018) showed that erastin, a ferroptosis (regulated necrotic cell death) inducer, synergized with cisplatin to increase its cytotoxicity in cancer cells via irreversible inhibition of Sx_c^-. In yet another interesting study, Liu et al. (2017) and Clemons, Liu, Duong, and Phillips (2017) discussed the importance of therapeutic strategies for targeting mutant p53 protein. One such strategy involved suppressing function of xCT along with APR-246, a small-molecule known to restore sequence-specific DNA binding of mutant p53 resulting in wild-type p53 transcriptional activity and tumor-suppressor function. This, beyond doubt, delineates the importance of xCT inhibitors in cancer treatment. Wang et al. (2017) studied the effects of propofol, a general anesthetic on proliferation and invasiveness of C6 glioma cells. The study successfully demonstrated the inhibitory effects (reduced cell viability, invasiveness, and migration coupled with decreased glutamate release) of propofol via Ca2+ permeable AMPA receptor (CPAR)—Sx_c^- pathway. Chen, Rauh, Buchfelder, Eyupoglu, and Savaskan (2017) and Chen et al. (2017) investigated the role of activating transcription factor 4 (ATF4) which critically regulates the oxido-metabolic state in gliomas in the pathogenesis of temozolomide (TMZ) (first-line treatment for malignant gliomas)-resistance. The authors found out that the TMZ treatment led to increased expression of ATF4, xCT among others and the elevation of xCT as a consequential event of ATF4 activation. The significance of the study was in identification of a promising strategy involving inactivation of ATF4 for abrogating chemoresistance and enhanced TMZ efficacy in human gliomas.

SSZ, a mutual prodrug of 5-aminosalicylic acid (5-ASA) and sulfapyridine, has been in therapy for ulcerative colitis due to its enzymatic breakdown in the gut. The highly polar and hydrophilc nature of **1** makes it poorly bioavailable (Robe et al., 2009). The randomized phase 1/2 trial of **1** for treating gliomas was an utter failure. Despite these facts, the interest of the scientific community in SSZ continued over all these years, Sehm et al. (2016) demonstrated that SSZ did not affect cell viability below 200 μM and above that it exhibited gliomatoxicity. It has been shown to (a) induce ferroptotic cell death in glioma cells, (b) potentiate the chemotherapeutic and autophagy-inducing activities of TMZ, and (c) reduced glioma-derived edema. Overall, SSZ has been viewed as a tumor microenvironment-normalizing drug.

Several researchers devoted substantial amount of time and efforts for developing potent, drug-like small-molecule Sx_c^- inhibitors. Patel et al. (2010) synthesized derivatives of α-amino-3-hydroxy-5-methyl-4-isoxazolepropionic acid (AMPA) and α-amino-3-carboxy-5-methyl-isoxazole propionic acid (ACPA) and analogs of **1** to evaluate their Sx_c^- inhibitory activity. Of all the synthesized molecules, amino acid naphthyl-ACPA and hydrazine carboxylic acid demonstrated similar potency as endogenous substrate, L-cystine, with K_i values 52, 64, and 59 μM, respectively, while corresponding isoxazolo[3,4-*d*] pyridazinones were far less potent. The molecules were designed essentially to mimic important structural features of **1**, including azo linkage. In yet another interesting study, Shukla et al. (2011) synthesized several analogs of **1** as potential Sx_c^- inhibitors. The individual drugs making up **1**, that is, 5-ASA and sulfapyridine exhibited half maximal inhibitory concentration (IC_{50}) values for Sx_c^--mediated cystine uptake >1,000 μM, while the corresponding value for **1** was 30 μM. In an attempt to replace the problematic azo linkage, several saturated and unsaturated linkers such as alkene, alkyne or the corresponding alkane, with the distal sulfapyridine moiety constant, yielded one equipotent (IC_{50} = 30 μM) and other less potent SSZ analogs, including **1** minus the pyridine sulfonamido compounds. Overall, the study mainly focused on replacing the azo linkage with other linkers. No attempt was made to explore the isosteres of the salicylic acid as well as the sulfapyridine moieties. Among these inhibitors, **1**, an approved anti-inflammatory drug, turned out to be a promising lead for further chemical optimization of potency and pharmacokinetic properties because it inhibited Sx_c^- with moderate potency and it lacked the adverse effects associated with approved anticancer drugs. However, SSZ is problematic due to its very poor systemic bioavailability (approximately 12%), rapid cleavage by colonic bacteria into inactive constituents and short half-life (~80 min). Its blood–brain-barrier (BBB) permeability is not known. It is likely to be prevented from crossing the BBB because it is so very hydrophilic and most importantly acidic. Acids are unlikely to cross BBB (Kharkar, 2014).

Careful examination of the molecular structure of **1** (Figure 1) reveals a lot of problematic features such as azo linkage (—N═N—), the pyridine ring, and salicylic acid moiety. Reduction of the azo

linkage by the intestinal bacteria yields potentially mutagenic structures (with anilino groups, sulfapyridine and 5-ASA). The salicylic acid moiety can undergo glucuronidation quickly during conjugation reaction. Even the highly anionic nature of the salicylic acid is likely to hamper membrane permeability during random-walk process, including BBB permeation. The literature reports indicated few relatively closer analogs of **1** being less potent. (Shukla et al., 2011). We thought of systematically maneuvering the SSZ structure in an attempt to arrive at a hit structure(s) which is tailor-made and preferably devoid of issues of **1**. In systematizing our design and synthesis efforts, we initiated our work with building a homology model of the xCT chain of Sx_c^- to rationally aid our design process. In the absence of the 3D structural information, the main emphasis was placed on building a comparative model of the antiporter which would overcome issues with similar, previously reported homology models (Matti et al., 2013). The developed homology model, after extended molecular dynamics simulations, was further used for molecular docking studies of the designed analogs of **1**.

In the present study, we report the homology model development of the Sx_c^- antiporter and provide an atomic description of SSZ-binding site. We also report the use of this model to guide the design of novel SSZ analogs along with their synthesis and in vitro biological evaluation in target-specific inhibition assays. Furthermore, we evaluated their cytotoxicity in patient-derived glial cell lines. Overall, the present investigation is a rational attempt to advance the design and development of novel Sx_c^- antiporter inhibitors as potential anticancer agents.

2 | MATERIALS AND METHODS

2.1 | Homology modeling of system x_c^- antiporter

To identify appropriate templates, the sequence of human cystine/glutamate transporter (Uniprot accession No. Q9UPY5) was submitted to homology recognition algorithms (threading servers) such as Homology detection & structure prediction (HHpred) by HMM-HMM comparison (http://toolkit.tuebingen.mpg.de/hhpred) (Söding, Biegert, & Lupas, 2005) AND LOMETS (Local MEta-Threading-Server) (http://zhanglab.ccmb.med.umich.edu/LO-METS/) (Wu & Zhang, 2007) for detecting remote homologies (Figure 2 and Figure S1S). We then used the structures of bacterial L-arginine/agmatine antiporter, AdiC open-to-out Arg^+ bound conformation (PDB code 3OB6) (Kowalczyk et al., 2011) and the outward-facing Arg^+-bound occluded (PDB 3L1L) (Gao et al., 2010) as templates for modeling the transmembrane domains. The substrate-free structures (apo) of ApcT, a broad-specificity amino acid transporter, and AdiC closely resembled each other with RMSD ~1.25 Å and, therefore, we modeled xCT in the fully occluded/inward facing conformation using apo-ApcT (PDB code 3GIA) (Shaffer, Goehring, Shankaranarayanan, & Gouaux, 2009) as reported previously (Gao et al., 2010).

Homology modeling was performed using MODELER-9v11 (Sali & Blundell, 1993) tool implemented in the UCSF Chimera (Pettersen et al., 2004). For the correct identification and positioning of the secondary structure elements, we started from the xCT and the templates alignment derived by the HHpred server. Hence, initially, backbone atom coordinates for transmembrane segments only were obtained from the relative coordinates of AdiC or ApcT. Subsequently, insertions and deletions were included and their backbones modeled. Loops were modeled on the basis of the structure of compatible fragments found in the PDB, and side chains were picked from a rotamer library using SCWRL4 (Krivov, Shapovalov, & Dunbrack Jr., 2009). Models were submitted to stepwise energy minimizations to reduce steric contacts (r.m.s. gradient = 0.01). Initially, hydrogens were minimized retaining the backbone and side chains fixed. The charges of side-chains were assigned at physiological pH. Minimizations were further carried by gradually realizing harmonic restraints on the side chains and keeping backbone fixed. In next step, harmonic restraints were only applied to the backbone. In the final step of minimization, the entire protein was treated as flexible. In this way, 50 initial models based on the CHARMM27 force field were generated, all sharing the same transmembrane topology but differing in local conformations. The quality of the models was evaluated by various diagnostics tools available on MolProbity webserver (Davis et al., 2007) and the Structural Analysis and Verification Server (SAVES, http://nihserver. mbi.ucla.edu/SAVES/) before and after the refinement step. The energetically most favorable models in apo (inward facing), open-occluded and open-out (Figure 3) conformations were selected for docking of the inhibitors.

2.2 | Docking studies

2.2.1 | Software

All the molecular modeling studies described herein were performed using Small-Molecule Drug Discovery Suite 2015–4 (Schrödinger Release 2015-4, 2015) and the modules included therein for performing various molecular modeling operations as described below.

2.2.2 | Protein structures

The developed homology models of xCT—apo, open-occluded and open-out—were subjected to *Protein Preparation* wizard using default settings as implemented in Schrödinger suite 2015–4 (Sastry, Adzhigirey, Day, Annabhimoju, & Sherman, 2013). The termini were capped. The H-bonds were optimized and, in the end, restrained minimization was performed wherein the heavy atoms were converged to root mean square deviation (RMSD) 0.3 Å. The prepared protein was then subjected to further minimization using Prime 4.2 (default settings) (Jacobson et al., 2004; Jacobson, Friesner, Xiang, & Honig, 2002; Halgren et al., 2004; Sastry et al., 2013). Glide version 6.9 (Friesner et al., 2004), as implemented in Schrödinger suite 2015–4, was used for performing docking studies of SSZ (**1**, Figure 1) and the designed molecules (Table 1).

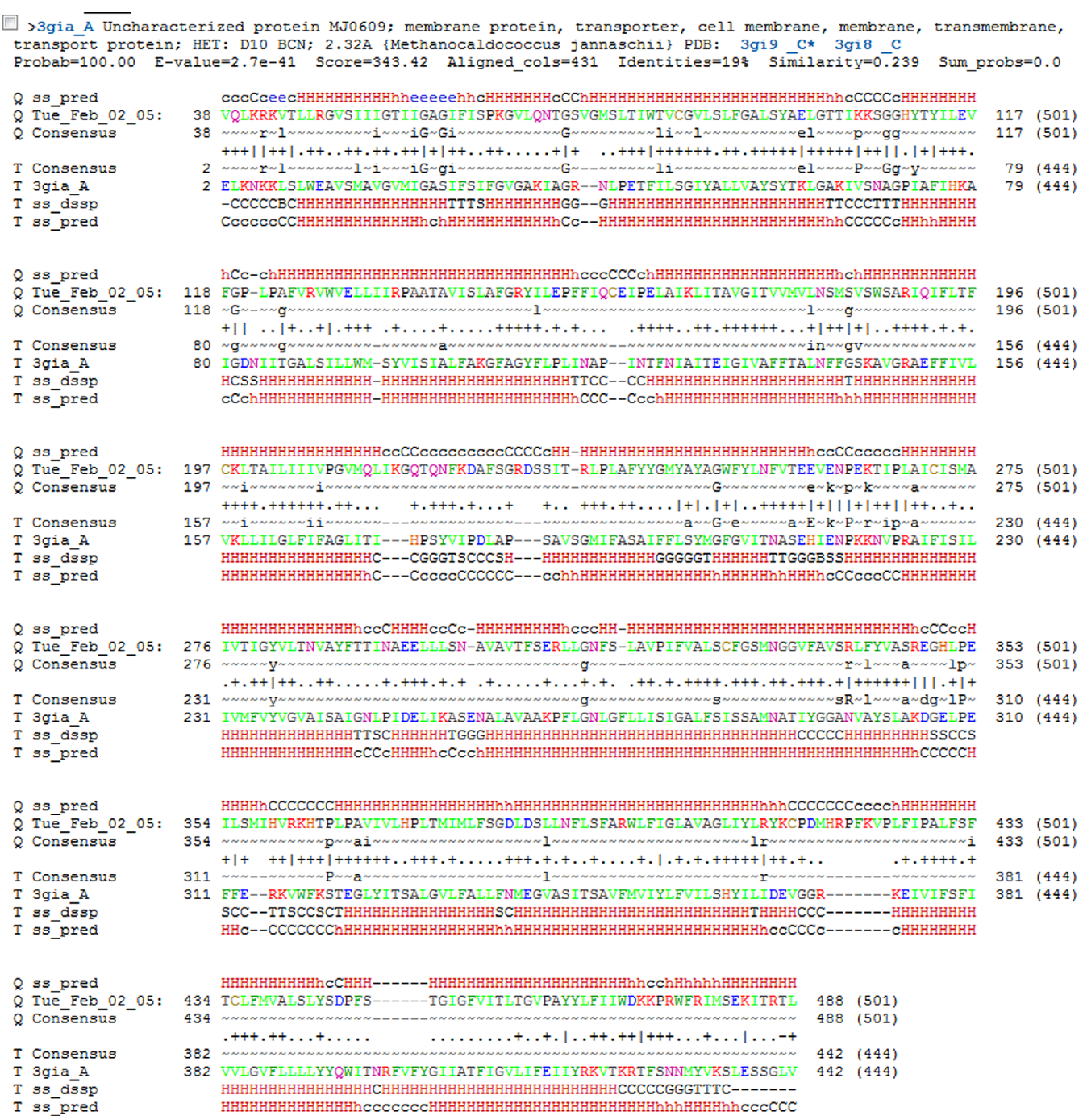

FIGURE 2 Sequence alignment of the xCT and apo ApcT, used for homology modeling. Sequences were aligned based on HMM profile alignment techniques such as HHpred. HHpred, Homology detection and structure prediction

2.2.3 | Ligand structures

The ligand structures were built in Maestro 10.4. All the structures were then optimized using the *LigPrep* version 2.6, as implemented in Schrödinger suite 2015–4 with default settings. Ligand preparation was followed by the docking studies. The study was aimed at investigating the binding modes of **1** (Figure 1) and few moderately potent inhibitors identified in this study.

2.2.4 | Receptor grid generation

The refined protein structures were used to define the ligand-binding pocket using *Receptor Grid Generation* module. The centroid of residue Arg396 was used for placing the enclosing box. The grid was then used for docking the ligands in the ligand-binding site. For docking studies, Extra Precision (XP) (Friesner et al., 2006) mode was used. The docked poses were minimized and RMSD to input ligand

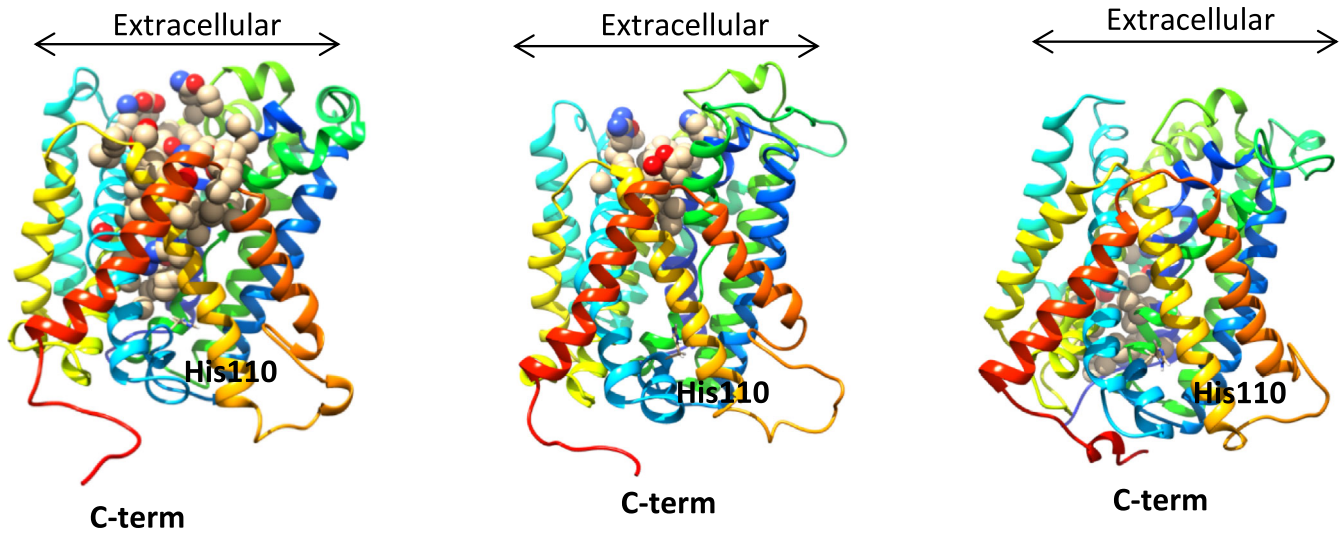

FIGURE 3 The conformation of the xCT ligand-binding site in (a) open-out conformation, (b) open-occluded conformation, and (c) inward-occluded conformation. His110 in the helix lies toward the cytosolic region

geometries were calculated. Table 1 lists the docking scores for all the molecules used in the docking studies along with interacting amino residues. Figure 4 shows the docking poses of representative molecules (**1**, **15**, and **12**) into the ligand-binding pocket of xCT. After docking studies, the pose viewer file was used for studying the binding modes of the ligands with the xCT chain of the antiporter. The docked posed of all other ligands in Table 1 are shown in Figures S4S (**4**), **S**5 (**5**), S6 (**7**), S7 (**11**), S8 (**14**), S9 (**18**), and S10 (**19**) (see Supporting Information section).

2.3 | Computational prediction of physicochemical and pharmacokinetic properties

The molecular/physicochemical properties for the designed molecules were calculated/predicted with the help of *Canvas* and *QikProp* modules of Schrödinger Small Molecule Drug Discovery Suite 2015–4. The compounds were first drawn in 2D, prepared using *LigPrep* module as per standard protocols. All the minimized structures were loaded into *QikProp* module and the physicochemical and pharmacokinetic properties were predicted.

2.4 | Molecular dynamics simulations

The molecular interactions were computed by Gromacs v5.0.4 (Abraham et al., 2015) and using the CHARMM36 force field as parameter (Pettersen et al., 2004). The CHARMM-GUI website (http://www.charmm-gui.org) was used to automate the system setup for MD simulation (Wu et al., 2014). Lipid bilayers models were built using a mixture of 1-palmitoyl-2-oleoyl-sn-glycero-3-phosphocholine (POPC) phospholipids using CHARMM-GUI membrane builder (Jo, Kim, & Im, 2007). The docked xCT-SSZ complex was placed in the rectangular simulation box and the preassembled bilayers were solvated with TIP3 water molecules. We have not taken into account the heterodimeric structure of Sx_c^- (Sato, Tamba, Ishii, & Bannai, 1999) because of the experimental data on interactions of xCT with the heavy chain, 4F2 is sparsely available (Palacín, Errasti-Murugarren, & Rosell, 2016). The activation, inactivation, and ion independent mechanism of the receptor are beyond the scope of this study. All protein residues were set to the standard CHARMM protonation states at neutral pH. The system was neutralized by adding NaCl as counterions and also adding a concentration of 150 mM. The simulation system had a dimension of approximately 93.1 Å × 93.1 Å × 120 Å and contained 96,593 atoms, including 208 POPC molecules, 20,477 CHARMM TIP3P water molecules, 79 Na^+ and 88 Cl^- ions (Figure 5).

The optimized protocol for running CHARMM simulations in GROMACS was used in this work (Lee et al., 2016). The structure was first energy-minimized for 5,000 steps using a steepest-descent algorithm with a tolerance of 1,000 kJ mol^{-1} nm^{-2}. The systems were then equilibrated by applying position restraints on the complex and NVT ensemble simulations for 400 ps at a temperature of 303 K. Subsequently, the built systems were further equilibrated without any restraints under semi-isotropic Berendsen pressure coupling. After the standard input builder minimization and equilibration steps, the production run of each simulation was performed or 600 ns. The van der Waal interactions were calculated with a force-based switch cut-off of 1.2 nm. Electrostatic corrections were made by Particle Mesh Ewald (PME) algorithm (Essmann et al., 1995), with 1.2 nm cut-off for Columbic interactions. All atom bond lengths were linked using the LINCS algorithm (Hess, Bekker, Herman, & Johannes, 1997) in conjunction with the simulation time step of 2 fs. In addition, the pressure was maintained at 1 bar. To maintain the temperature, a Nosé–Hoover temperature coupling method (Hoover, 1985; Nosé, 1984; Parrinello & Rahman, 1981) with a tau-t of 1 ps was used, and for pressure coupling, a semi-isotropic Parrinello–Rahman method

TABLE 1 In vitro system x_c^- antiporter inhibition, cytotoxicity and summary of docking analyses of the title compounds in the ligand-binding site of modeled xCT

Molecule	Structure	IC_{50} (μM) (Sx_c^- Inhibition[a])	IC_{50} (μM) Cytotoxicity[b,c,d]	XP GScore	Interacting residues in the ligand-binding pocket[e]
1	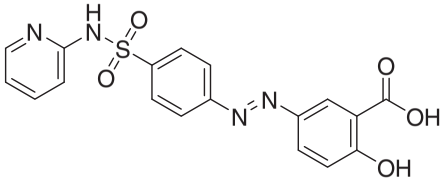	76.70 ± 7.46	100.3 ± 6.5[b] >800[c] 78.2 ± 11.9[d]	−6.972	**Arg396**, **Thr56**, **Asn390**, Ala138, Tyr241, Tyr244, Leu392, Leu389, Trp397, Tyr240
4	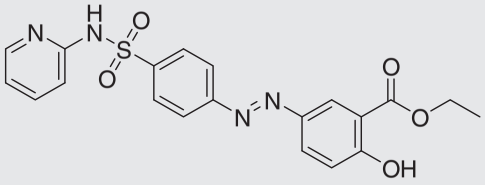	111.05 ± 8.97	38.24 ± 4.7[b] 565.9 ± 22.5[c] 53.04 ± 6.2[d]	−7.094	**Arg396**, **Arg135**, Ala247, Phe250, Tyr241, Tyr244, Leu389, Trp397
5	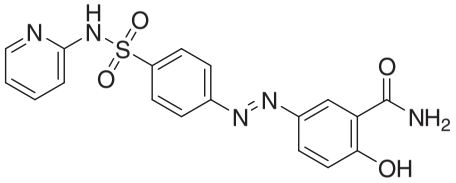	132.95 ± 10.34	73.65 ± 8.2[b] >800[c] 48.71 ± 6.9[d]	−6.830	**Arg396**, **Arg135**, **Ser330**, Ala247, Tyr240, Tyr244, Leu389, Trp397
7	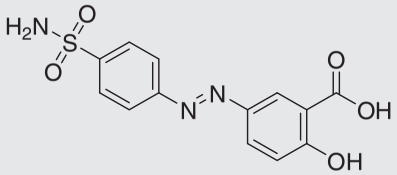	>500	N.D.	−5.665	**Arg396**, **Thr56**, Tyr244, **Ser393**, Tyr240, Leu389, Trp397
11	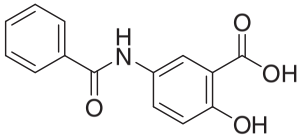	>500	N.D.	−6.299	**Arg396**, **Arg135**, Ala247, Tyr241, Tyr244, Leu392, Ile142
12	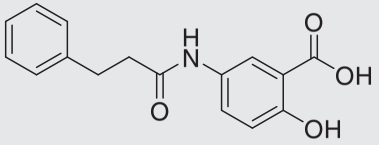	138 ± 11.51	823.1[b] >800[c] >500[d]	−5.755	**Arg396**, **Arg135**, Ala138, Ile57, Tyr244, Phe250, Ala245, Ala60

(Continues)

TABLE 1 (Continued)

Molecule	Structure	IC_{50} (μM) (Sx_c^- Inhibition[a])	IC_{50} (μM) Cytotoxicity[b,c,d]	XP GScore	Interacting residues in the ligand-binding pocket[e]
14	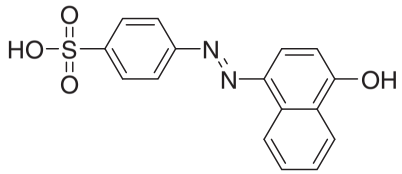	>500	N.D.	−4.973	**Arg396**, **Arg135**, Ala138, Ile134, Tyr244, Tyr241, Ala245, Leu392
15	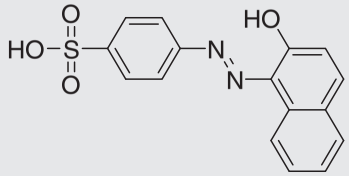	116.74 ± 7.11	137.8±[a] >800[b] 77.13 ± 18.22[d]	−7.073	**Arg396**, **Arg135**, Ala138, Ile134, Tyr244, Tyr241, **Ile57**, Ala245, Leu392
18	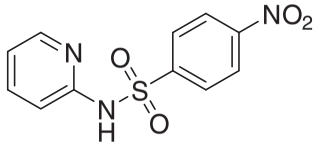	170.71 ± 8.23	N.D.	−2.436	**Arg396**, Ala138, Tyr244, Tyr241, Ile57, Ala245, Leu392, Leu398
19	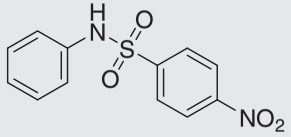	273.14 ± 12.33	169.1 ± 7.84[b] 658.1 ± 22.39[c] 112.3 ± 21.27[d]	−4.678	**Tyr244**, Tyr241, Ile57, Ala245, Ala247, Leu389, Ile58, Trp397

Abbreviations: N.D, not determined; s.d, standard deviation.

[a]C6 Cell lines, n = 3, Mean ± s.d.

[b]U87MG cell lines, *n* = 3, Mean ± s.d.

[c]SF268 cell line, *n* = 3, Mean ± s.d.

[d]C6 cell line, *n* = 3, Mean ± s.d.

[e]H-bonding residues in bold face.

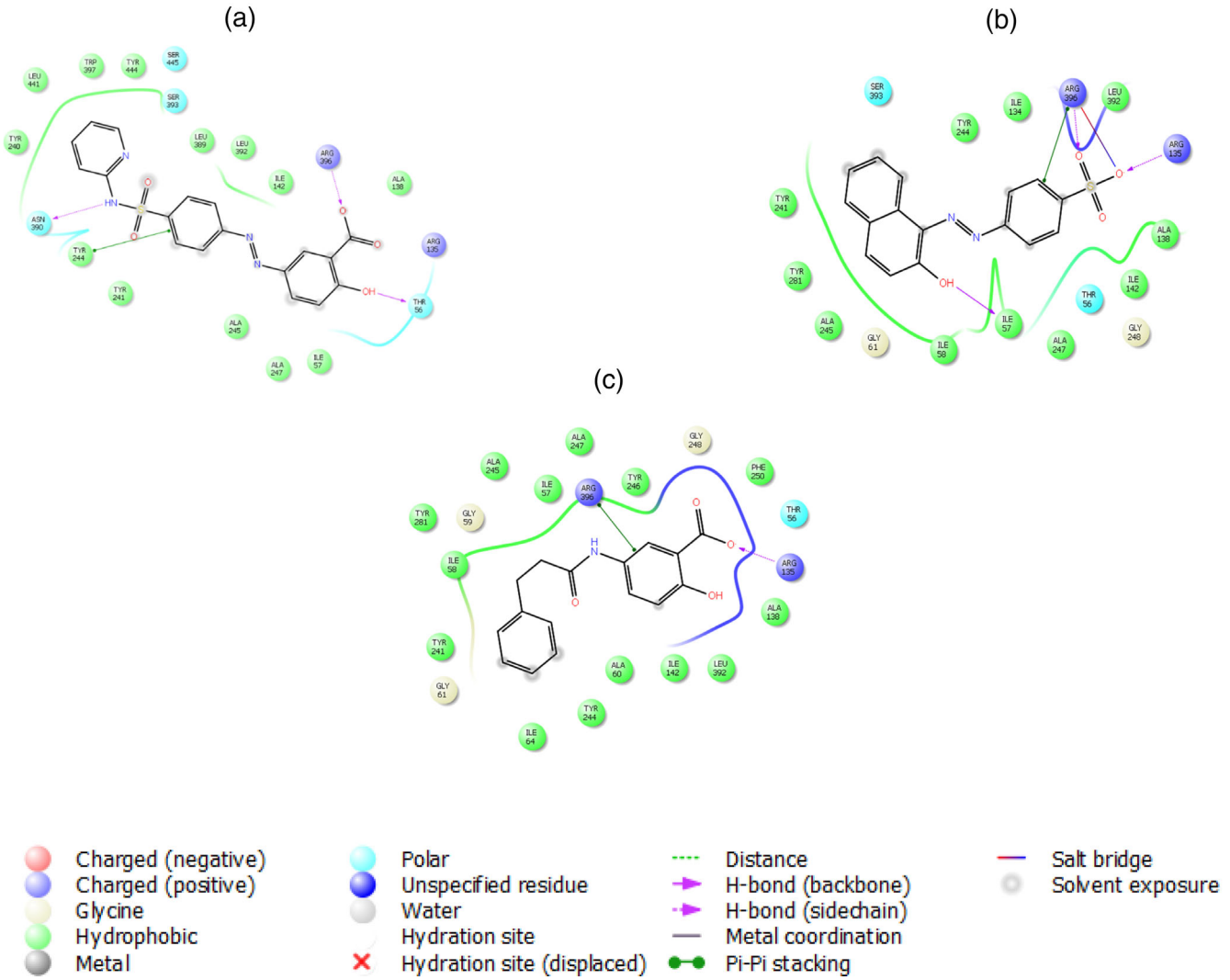

FIGURE 4 Binding mode of **1**, **15**, and **12** in the ligand-binding site of Sx_c^- antiporter; (a) 2D representation of the drug (**1**)—transporter interactions depicting H-bonds, π–π stacking and hydrophobic interactions; (b) 2D representation of ligand (**15**)—antiporter interaction, and (c) 2D representation of ligand (**12**)— antiporter interaction. 2D, two-dimensional

(Nosé, 1984; Nosé & Klein, 1983) with a tau-p of 5 ps and a compressibility of 4.5×10^{-5} bar^{-}1 was used.

The trajectory was subjected for analyses of secondary structure, root mean square deviation (RMSD) on the backbone atoms of protein, all atoms of the binding site and heavy atoms of ligands using AMBERTools16 (Case et al., 2016). Hydrogen bonds, native (any atoms that are closer than 7 Å in the specified reference docked pose) and nonnative contacts of the protein within 7 Å from the ligand and clustering analyses were also performed. A hydrogen bond between a donor (D–H) and a heavy acceptor atom (A) was considered to be formed when the A to D distance was <3.0 Å and the A-H-D angle is greater than the angle cut-off of 135°. These geometric criteria for defining hydrogen bonds are consistent with those used in prior studies. Secondary structure content was assessed with the DSSP algorithm. Visualization was carried out using UCSF Chimera (Pettersen et al., 2004) and Discovery Studio 4.1.

2.4.1 | Cavity-volume calculator

The volume of the SSZ cavity was calculated by POVME (Durrant, Votapka, Sørensen, & Amaro, 2014). The xCT snapshots were extracted from the trajectory every frame (60,000 frames in total from 600 ns) and superimposed onto the reference structure with a pregenerated 3D-grid representing the SSZ cavity. The volume was calculated by counting the grid points located within 10 Å in the SSZ-cavity.

Clustering analysis of the trajectory obtained from MD simulation was performed using CPPTRAJ of Amber Tools 16 with the hierarchical agglomerative algorithm and average-linkage approach and cluster size set to 10, to determine various populations of interactions of SSZ with the receptor, water, and ions in the cavity. Cluster analysis of 30,000 frames saved at 20-ps intervals during the 0–600 ns period was done by aligning the first root mean square coordinate deviation on the backbone of xCT residues and then by clustering based on the

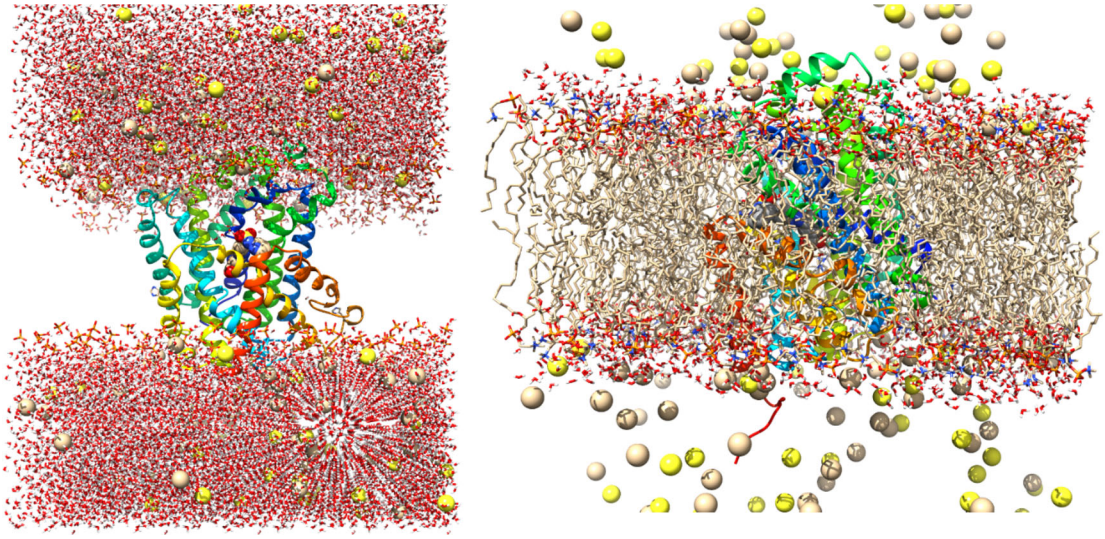

FIGURE 5 Schematic representation of protein–ligand complex embedded in the POPC bilayer. Water molecules and lipids are shown as sticks, the protein in ribbon colored from N- (blue color) to C-terminal (red) and the ions as spheres. Sulfasalazine is shown in van der Waals spheres with the receptor shown in a representative snapshot taken from the top eight clusters

movement of the ligand with respect to the last RMS-fit (in this case the backbone atoms of residues xCT).

2.5 | Chemistry

2.5.1 | General

All the solvents (including dry solvents) and chemicals were procured from commercial suppliers such as Sigma-Aldrich Chemical Corporation (St. Louis, MO), Fischer Scientific (Hampton, NH), and VWR International (Radnor, PA), and were used as received unless otherwise indicated. All reactions were performed under an inert atmosphere (N_2) unless otherwise noted. Analytical silica gel 60 F_{254}-coated TLC plates were purchased from Merck Millipore (Billerica, MA) and were visualized with UV light or by treatment with TLC reagents such as ninhydrin, Dragandorff's or phosphomolybdic acid (PMA). Flash-column chromatography was carried out on Combiflash R_f (Lincoln, NE) using silica gel (230–400 mesh). ^{1}H-NMR spectra were routinely recorded on Bruker 400 MHz FT-NMR (Billerica), with tetramethylsilane (TMS) as an internal standard. Mass spectra were obtained using Agilent LCMS, 6110AA model (Santa Clara, CA). Reversed-phase HPLC (RP-HPLC) analyses were performed using Agilent HPLC instrument (Santa Clara) equipped with PDA absorption detector. Melting points were recorded using Veego Instruments, VMP-DS model, capillary melting point apparatus (Mumbai, Maharashtra, India) and are uncorrected. Radioactivity was measured by Hidex-Triathler Liquid Scintillation Counter (Brandon, FL). [^{35}S]L-cystine was purchased from BRIT (Mumbai).

2.5.2 | Synthetic schemes

The synthetic route leading to compounds **4** and **5** is shown in Scheme 1. Esterification of **1** resulted in **4**, which upon further amidation led to **5**. In Scheme 2, diazotization of sulphanilamide (**6**) followed by coupling with salicylic acid resulted in **7**. Amides were synthesized according to Scheme 3. The —COOH group of **8** was protected as an ester to give **9** which on further reaction with different aromatic acids gave corresponding amides **15a** and **15 h** along with the acylated phenolic impurities. The ester derivatives (**15a** and **15 h**) and their acylated phenolic impurities were further subjected to hydrolysis using LiOH.H_2O to give the corresponding acids **11** and **12**. In another diazotization reaction (Scheme 4), 4-aminobenzensulfonic acid (**13**) on diazotization followed by coupling with α- and β-naphthols yielded **14** and **15**. Sulfonamides (**18** and **19**) were synthesized by reaction of p-nitrobenzenesulfonyl chloride (**16**) with aromatic amines (**17a** and **17b**) (Scheme 5).

2.5.3 | Synthesis of ethyl 2-hydroxy-5-[(E)-2–4 {4-[(pyridine-2-yl)sulfamoyl]phenyl}diazen-1-yl]-benzoate (4)

A mixture of **1** (0.5 g, 10 mmol), absolute EtOH (10 mL) and conc. H_2SO_4 (1 mL) was boiled under reflux with stirring for 8.5 hr followed by evaporation to dryness. Water (5 mL) was added to the residue and the mixture filtered. The filtrate was basified with saturated $NaHCO_3$ solution and the precipitated solid was collected by filtration. The filtrate was extracted with DCM and the solvent evaporated to dryness. The residue was triturated with petroleum ether (40–60 °C) and filtered to yield **4** as yellow solid (0.46 g, 87%). R_f: 0.68 ($CHCl_3$/MeOH═9:1); IR (KBr): ν═3,417 (m; ν[O—H]), 3,203 (s; ν[N—H]), 2,926 (m; ν[C—H_{Alipha}]), 2,385 (m; ν[N═N]),1,685 (s; ν[C═O]), 1,295 (s; ν[S—O] cm^{-1}; ^{1}H-NMR (400 MHz, DMSO-d_6): δ (ppm) 11.1 (s, 1H), 8.32 (d, 1H), 8.0–8.1 (m, 3H), 7.92–7.99 (m, 3H), 7.75 (t, 1H), 7.17–7.25 (m, 2H), 6.85 (t, 1H); 4.41, (q, 2H), 1.40 (t, 3H); LC–MS (ESI): 427.1 $[M + H]^+$; Melting point: 213 °C; Elemental analysis calculated (%) for $C_{20}H_{18}N_4O_5S$: C 56.33, H 4.25, N 13.14; Found: C 56.72, H 4.11, N 12.92.

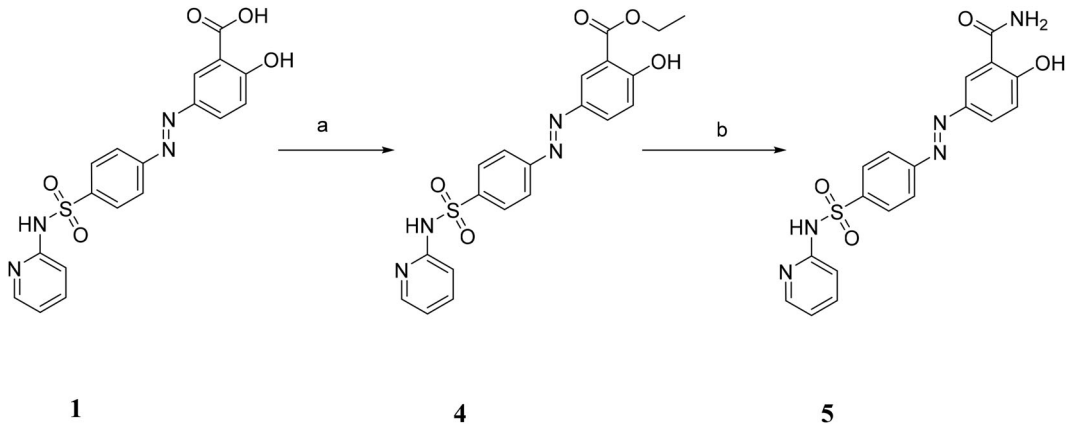

SCHEME 1 Reagents and conditions: (a) EtOH, H_2SO_4, RT; (b) EtOH, NH_3, RT

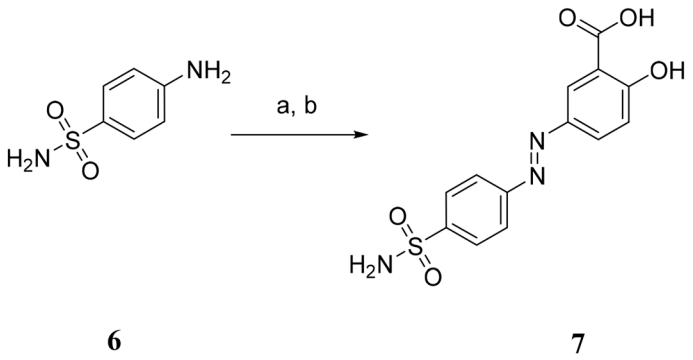

SCHEME 2 Reagents and conditions: (a) conc. HCl, $NaNO_2$, 0–5 °C; (b) salicylic acid, NaOH, 0–5 °C

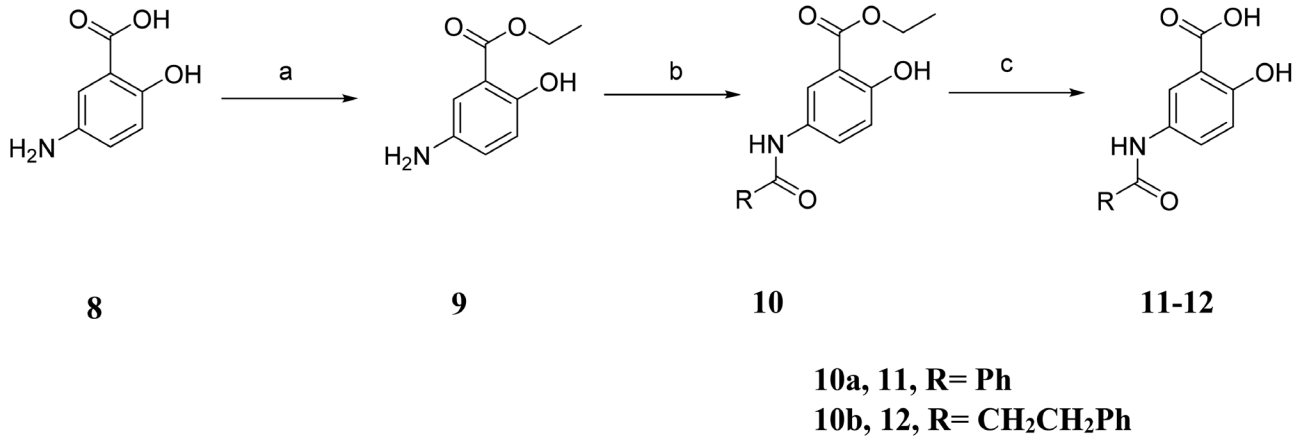

SCHEME 3 Reagents and conditions: (a) EtOH, H_2SO_4, reflux; (b) (i) 1-[bis(dimethylamino)methylene]-1H-benzotriazolium 3-Oxide Tetrafluoroborate (TBTU), di-isopropyl ethylamine (DIPEA), (ii) benzoic acid, (iii) hydrocinnamic acid, DCM; (c) LiOH.H_2O, tetrahydrofuran-methanol (THF-MeOH)

2.5.4 | Synthesis of 2-Hydroxy-5-[(E)-2-{4-[(pyridine-2-yl)sulfamoyl]phenyl}diazen-1-yl]benza-mide (5)

Compound **4** (0.3 g, 0.7 mmol) was dissolved in EtOH (20 mL). The reaction mixture was saturated with NH_3 gas and further kept for 24 hr. The reaction was monitored with TLC for completion. The reaction mixture was filtered to collect yellow solid (0.15 g, 58%). R_f: 0.51 ($CHCl_3$); IR (KBr): ν=3,425 (m; ν[O—H]), 3,199 (s; ν[N—H]), 2,993 (m; $\nu[C—H_{Alipha}]$), 2,361 (m; ν[N═N]), 1,685 (s;ν[C═O]), 1,388 (s;ν[S—O]) cm^{-1}; ^{1}H-NMR (400 MHz, DMSO-d_6): δ (ppm) 13.8 (brs, 1H), 8.72 (brs, 1H), 8.6 (d, 1H), 8.12 (s, 1H), 8.05–8.09 (m, 2H), 7.95–8.0

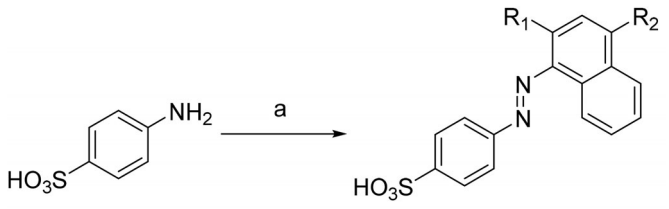

13

14, R_1 = H, R_2 = OH
15, R_1 = OH, R_2 = H

SCHEME 4 Reagents and conditions: (a) (i) conc. HCl, $NaNO_2$, 0–5 °C; (ii) aq. NaOH, (1) α-naphthol or (2) β-naphthol, 0–5 °C

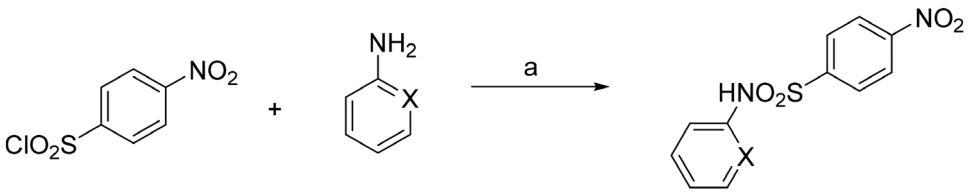

16

17a, X = N
17b, X = CH

18, X = N
19, X = CH

SCHEME 5 Reagents and Conditions: (a) pyridine, 80 °C

(m, 2H), 7.9–7.94 (m, 2H), 7.74–7.8 (t, 1H), 7.2 (d, 1H), 7.05–7.09 (d, 1H), 6.85–6.9 (t, 1H); LC–MS (ESI): 397.1 $[M + H]^+$; Melting point: 190–192 °C. Elemental analysis calculated (%) for $C_{18}H_{15}N_5O_4S$: C 54.40, H 3.80, N 17.62; Found: C 54.18, H 3.39, N 17.28.

2.5.5 | General procedure for synthesis of 7, 14–15 (Method A)

Respective amines along with $NaNO_2$ (0.13 g, 15 mmol) were dissolved in of water (1.5 mL) and maintained at 0–5°C. Conc. HCl (1.5 mL) diluted with water (1.5 mL) maintained at 0–5 °C was then added to the above mixture. After 10 min. Stirring (0–5 °C), the solids in the above mixture were filtered and added to respective phenols (5.4 mmol) dissolved in 2.5 M NaOH (10 mL) and stirred at 0–5 °C. After 10 min., conc. HCl (1.5 mL) was added and allowed to stir for 45 min at 0–5°C. NaCl (1 g) was then added to the reaction mixture and heated until all the solids dissolved. The reaction was monitored by TLC for completion. The reaction mixture was cooled at RT and then on an ice bath for 15 min. Solids were filtered and air dried. The crude product was purified by recrystallization from EtOH to give title compound.

2.5.6 | Synthesis of 2-Hydroxy-5-[(E)-2-[4-sulfamoylphenyl]diazen-1-yl]benzoic acid (7)

Compound **7** was obtained as red solid (1.1 g, 63%) by diazotization reaction of **6** (1 g, 5 mmol) with salicylic acid (0.76 g, 5 mmol) as described in Method A. R_f: 0.4 ($CHCl_3$/MeOH═8:2); IR (KBr): ν═3,367 (w; ν[O—H]), 3,199 (m; ν[N—H]), 2,369 (w; ν[N═N]), 1,685 (s; ν[C═O]), 1,299 (s; ν[S—O]) cm^{-1}; ^{1}H-NMR (400 MHz, DMSO-d_6): δ (ppm) 8.38 (d, 1H), 8.14–8.20 (dd, 1H), 8.0 (m, 4H), 7.5 (m, 2H), 7.16–7.18 (d, 1H); LC–MS (ESI): 322.14 $[M + H]^+$; Melting point: 264–266 °C; Elemental analysis calculated (%) for $C_{13}H_{11}N_3O_5S$: C 48.49, H 3.45, N 13.08; Found: C 48.13, H 3.05, N 13.35.

2.5.7 | Synthesis of 4-[(E)-2-(4-Hydroxynaphthalen-1-yl)diazen-1-yl]benzene-1-sulfonic acid (14)

Reaction of **13** (0.49 g, 2.8 mmol) following diazotization with α-naphthol (0.38 g, 2.8 mmol) as described in method A resulted in compound **14** as brown solid (0.4 g, 47%). Rf: 0.33 ($CHCl_3$); IR (KBr): ν =3,430 (s; ν[O – H]), 2,362 (m; ν[N=N]), 1,652 (w;ν[C-H Ar]), 1,173 (s; ν[S – O]) cm^{-1}; ^{1}H-NMR (400 MHz, DMSO-d_6): δ (ppm) 8.7 (d, 2H), 8.15 (d, 1H), 8.01 (d, 1H), 7.6–7.8 (m, 4H), 7.5 (m, 2H), 7.3 (t, 1H), 6.42 (d, 1H); LC–MS (ESI): 329.1 [M + H]+. Melting point >300°C; Elemental analysis calculated (%) for $C_{16}H_{12}N_2O_4S$: C 58.53, H 3.68, N 8.53; Found: C 58.42, H 3.60, N 8.24.

2.5.8 | Synthesis of 4-[(E)-2-(2-Hydroxynaphthalen-1-yl)diazen-1-yl]benzene-1-sulfonic acid (15)

Compound **15** was obtained as orange solid (0.72 g, 81%) by reaction of diazotised **13** (0.49 g, 2.8 mmol) with β-naphthol (0.38 g, 2.8 mmol) as described in method A. R_f: 0.39 ($CHCl_3$); IR (KBr): ν = 3,429 (s; ν[O—H]), 2,356 (m; ν[N═N]), 1,661 (w;ν[C—H_{Ar}]), 1,195 (s; ν[S—O]) cm^{-1}; ^{1}H-NMR (400 MHz, DMSO-d_6): δ (ppm) 15.8 (s, 1H), 8.55 (d, 1H), 7.92 (d, 1H), 7.79 (d, 2H), 7.75 (s, 1H), 7.71 (d, 2H), 7.60 (t, 1H), 7.41 (t, 1H), 6.46 (d, 1H); LC–MS (ESI): 327.05 $[M–H]^–$; Melting point >300 °C; Elemental analysis calculated (%) for $C_{16}H_{12}N_2O_4S$: C 58.53, H 3.68, N 8.53; Found: C 58.16, H 3.62, N 8.29.

2.5.9 | General procedure for the synthesis of 18–19 (Method B)

4-Nitrobenzenesulfonyl chloride was dissolved in pyridine (15 mL). Respective amines (4 mmol) were added to above solution and stirred for 2 hr at 80 °C. The reaction was monitored by TLC. The excess of pyridine was removed by washing with water (30 mL) yielding crude solid product.

2.5.10 | Synthesis of 4-nitro-N-(pyridine-2-yl) benzene-1-sulfonamide (18)

Compound **18** was obtained as creamy white solid (0.76 g, 60%) from **16** (1 g, 4 mmol) and **17a** (0.38 g, 4 mmol) as described in Method B. R_f: 0.52 ($CHCl_3$/MeOH = 9:1); IR (KBr): ν =2,930 (m; ν[N—H]), 1,514 (w; ν[N—O]), 1,130 (s;ν[S—O]) cm^{-1}; ^{1}H-NMR (400 MHz, DMSO-d_6): δ (ppm) 11.17 (s, 1H), 8.42 (d, 1H), 8.33 (d, 2H), 8.15–8.25 (m, 3H), 7.85 (t, 1H), 7.16 (t, 1H); LC–MS (ESI): 278 $[M-H]^-$; Melting point: 192 °C; Elemental analysis calculated (%) for $C_{11}H_9N_3O_4$: C 47.31, H 3.25, N 15.05; Found: C 47.20, H 3.05, N 14.85.

2.5.11 | Synthesis of 4-nitro-N-phenylbenzene-1-sulfonamide (19)

Compound **19** was obtained as creamy white solid (0.84 g, 65%) from **16** (1 g, 4 mmol) and **17b** (0.37 g, 4 mmol) as described in Method B. R_f: 0.62 ($CHCl_3$/MeOH = 95:5); IR (KBr): ν = 3,127 (m; ν[N—H]), 1,511 (s; ν[N—O]), 1,147 (s;ν(S—O)) cm^{-1}; ^{1}H-NMR (400 MHz, DMSO-d_6): δ (ppm) 10.6 (s, 1H), 8.33 (d, 2H), 7.94 (d, 2H), 7.21–7.28 (t, 2H), 7.05–7.12 (m, 3H); LC–MS (ESI): 277 $[M-H]^-$; Melting point: 153 °C; Elemental analysis calculated (%) for $C_{12}H_{10}N_2O_4S$: C 51.79, H 3.62, N 10.07; Found: C 51.42, H 3.58, N 10.40.

2.5.12 | General procedure for synthesis of 11–12 (Method C)

5-Aminosalicylic acid (15 g, 97 mmol), absolute EtOH (250 mL) and 7.5 mL conc. H_2SO_4 were refluxed with stirring for 8.5 hr followed by evaporation to dryness. Water (20 mL) was added to the residue and the mixture was filtered. The filtrate was basified with saturated bicarbonate solution and solids were collected by filtration. The filtrate was extracted with DCM and evaporated to dryness. The residues were triturated with petroleum ether (40–60 °C) and filtered to give ethyl 5-amino-salicylate. This compound (0.5 g, 2.76 mmol) was dissolved in DMF (10 mL) along with aromatic acids (1 eq) and TBTU (1 eq) followed by stirring at 0 °C. Diisopropylethyl amine (5 eq) was then added dropwise and kept at RT overnight. The reaction was monitored by TLC. The reaction mixture was partitioned between EtOAc and water. The dried organic layers were evaporated to get crude product, which was further dissolved in THF:MeOH (1:1) and LiOH.H_2O (1 eq) was added to the reaction flask. The reaction was monitored by TLC. The reaction mixture was acidified with 1 N HCl and the precipitated solids were filtered, washed with cold water and air dried.

2.5.13 | Synthesis of 5-Benzamido-2-hydroxybenzoic acid (11)

Reaction of **9** (0.5 g, 2.76 mmol) and benzoic acid (0.33 g, 2.76 mmol) formed **10a** which was further hydrolysed to obtain **11** as brown solid (0.054 g, 27%) as described in general method C. R_f: 0.4 ($CHCl_3$/MeOH = 9:1); IR (KBr): ν = 3,287 (s; ν[N—H]), 1,664 (s; ν[C═O Acid]), 1,528 (s; ν[C═O Amide]) cm^{-1}; ^{1}H-NMR (400 MHz, DMSO-d_6): δ (ppm) 14.1 (brs, 1H), 11.1 (brs, 1H), 10.2 (s, 1H), 8.25 (d, 1H), 7.91 (d, 2H), 7.82 (dd, 1H), 7.52 (m, 2H), 7.45 (m, 1H), 6.93 (d, 1H); LC–MS (ESI): 316.1 $[M + H]^+$; Melting point: 197 °C; Elemental analysis calculated (%) for $C_{14}H_{11}NO_4$: C 65.37, H 4.31, N 5.44; Found: C 64.96, H 4.21, N 5.39.

2.5.14 | Synthesis of 2-Hydroxy-5-(3-phenylpropanamido)benzoic acid (12)

Reaction of **9** (0.5 g, 2 mmol) and hydrocinnamic acid (0.5 g, 2.76 mmol) formed **10b** which was further hydrolysed to obtain **12** as white solid (0.066 g, 33%) as described in general method C. R_f: 0.21 ($CHCl_3$/MeOH = 9:1); IR (KBr): ν = 3,265 (s; ν[N—H]),1,640 cm–^{1} (s; ν[C═OAcid]), 1,569 (s;ν[C═OAmide]) cm^{-1}; ^{1}H-NMR (400 MHz, DMSO-d_6): δ (ppm) 14.0 (brs, 1H), 11.1 (brs, 1H), 9.85 (s, 1H), 8.10 (d, 1H), 7.62 (dd, 2H), 7.24 (m, 4H), 7.15 (t, 1H), 6.85 (d, 1H), 2.90 (t, 2H), 2.50 (t, 2H) ; LC–MS (ESI): 286.2 $[M + H]^+$; Melting point: 211 °C; Elemental analysis calculated (%) for $C_{16}H_{15}NO_4$: C 67.36, H 5.30, N 4.91; Found: C 67.21, H5.21, N 4.69.

2.6 | Biology

2.6.1 | In vitro Sx_c^- inhibition assay ([^{35}S]L-Cystine uptake assay)

Uptake assay was performed as reported earlier by Liu, Rush, Zapata, and Lobner (2009) with a few modifications. Briefly, 12×10^4 cells/mL were seeded in 96-well plates and incubated (5% CO_2, 37 °C) for 24 hr. Media were removed and cells were washed with uptake buffer. Immediately after washing, [^{35}S] L-cystine (5 μCi/mL) was exposed to cells along with title compounds and unlabeled cystine for 3 min. Duration. [^{35}S]L-cystine present in the extracellular environment was washed with ice-cold PBS. Radioactivity was measured after dissolving the cells using 0.3 N NaOH. Values were normalized to positive blank which contained exposure of [^{35}S]L-cystine to cells in the absence of synthesized compounds.

2.6.2 | In vitro anticancer assay

Cytotoxicity of moderately active Sx_c^- inhibitors (**4**, **5**, **12**, **15** and **19**) was evaluated using MTT assay on three of the glioblastoma cell lines: U87 MG (human), SF268 (human) and C6 (mouse) (van de Loosdrecht,

Beelen, Ossenkoppele, Broekhoven, & Langenhuijsen, 1994). Briefly, 3,000 cells were seeded in each of the 96-well plates for different concentration of six compounds ranging from 10 μM to 1,000 μM. After 18 hr of seeding, different drug concentrations were added into the cells along with DMSO (vehicle control). Following 48 hr of incubation with the compounds, cells were incubated with MTT reagent (5 mg/mL) for 4 hr in incubation and the crystals were solubilized using DMSO. The absorbance was then measured at 570 nm using SPECTROstar Nano Microplate Reader. The IC_{50} values for the title compounds were determined using GraphPad prism software using nonlinear regression analysis.

3 | RESULTS AND DISCUSSION

3.1 | Homology modeling

3.1.1 | Selection of suitable templates for model building

Threading methods returned AdiC and ApcT as the best and the only reliable templates. Metrics indicating the reliability of structural relation were unambiguous: both servers yielded the highest possible confidence value despite sequence identity of less than 21% between xCT and AdiC/ApcT (Figure 2 and Figure 1S). Furthermore, both proteins have antiporter activity, are ion independent, and are L-amino acid transporters. Thus, HHpred server estimated the probability (i.e., the degree of confidence) of homology between the entire transmembrane domains (TMD) of AdiC and ApcT as 100%. This remarkably high score was statistically supported by notable E-value ($1E^{-45}$ for AdiC and $2.7E^{-41}$ for ApcT) and *p*-value ($2.7E^{-50}$ for AdiC and $7.3E^{-46}$ for ApcT) scores. LOMETS, which takes predictions from nine different servers that represent a diverse set of state-of-the-art threading algorithms, also ranked AdiC and ApcT as top-two templates. These servers also predicted glutamate/γ-aminobutyrate (GABA) antiporter; LEUT, glutamate-GABA antiporter as a suitable template (based on E and *p* values), but we did not use this template to model xCT because the sequence identity dropped below 15%.

The researchers at the University of Montana used ClustalW alignment method to thread xCT model using the apo structure of ApcT (Matti et al., 2013). We expect significant differences in the conformation of active site owing to the differences in the alignment methods and the availability of newer templates in holo- and apo-conformations. Profile HMMs make allowance for amino acid and insertion/deletion frequencies, and thus, for the importance of each position for defining protein homologies. Pair-wise comparison of profile HMMs is currently considered the most powerful and accurate method for detecting and aligning remotely related sequences and a method like HHPRED also takes into account secondary structure prediction (Söding, 2005). In conclusion, two quantitative estimates (HHpred and LOMETS metaserver) converge to the same conclusion, indicating that AdiC and ApcT are the best available and highly useful templates for homology modeling of xCT.

3.1.2 | Threading

In this study, three homology models of the human xCT were constructed in outward-open, outward-occluded and inward-occluded conformations based on AdiC and ApcT crystal structures (PDB ID 3OB6, 3L1L, and 3GIA, respectively). The stereochemical quality of the threaded models, both before and after energy refinements, were evaluated using the Molprobity and SAVES server which uses PROCHECK, ERRAT and VERIFY 3D programs (Table S1S). Molprobity analyses showed the absence of poor rotamers, cβ deviations, and bad bonds and angles in all three models. The outlier residues shown in Ramachandran plot were not refined because the residues did not constitute part of the active site. The VERIFY 3D scores were lower for the refined structures than the templates, but acceptable.

3.1.3 | Main structural features

The homology models derived from AdiC and ApcT conform to the characteristic fold of the SLC7 families of amino acid transporters: the model comprises of 12 transmembrane all-helical segments with the N- and C-termini located inside the cell (Fotiadis, Kanai, & Palacin, 2013). The substrate-binding site is quite hydrophobic. Residues His110 and Thr112 are at the surface and are close to the substrate-binding/permeation pathway of xCT. Cys327 seats right near the extracellular hydrophobic cavity whereas His110 is at the top of Arg396. Structural alignment of the models based on substrate-free and substrate-bound templates revealed major conformational changes in TM2, TM6, TM8, and TM10. Transmembrane domain 8 is straight in the outward-open structure and kinked in the inward-open model and this is in agreement with the previous result for AdiC and ApcT (Jeschke, 2013).

The Computed Atlas of Surface Topography of proteins (CASTp) web server (Dundas et al., 2006) was used to locate, measure, and characterize the pockets on the protein surfaces for all three models and the voids in the interior of proteins. The molecular surface volume and area calculated by CASTp for all models are reported in Table S2 The binding pocket of the models based on open-out and open-occluded conformations is widely open toward the extracellular side (Figure 3), reflected by the larger mouth volume compared to that of the model based on the apo structure.

3.2 | Predicted physicochemical and pharmacokinetic properties

As represented in Table 2, most of the designed compounds possessed acceptable molecular, physicochemical, and pharmacokinetic properties such as logD, logS@ pH 7.4, #H-bond donors and acceptors as well as TPSA and #rotatable bonds. Most of the designed molecules had TPSA of ~100 $Å^2$ and few exhibited $logD_{7.4} > 2.5$, indicating that these molecules (including masked acid, **4**) were likely to be orally absorbed and may potentially gain entry through BBB. The calculation/predictions of molecular properties was performed to eliminate designs likely to fail down the line due to unacceptable properties.

TABLE 2 [a]Physicochemical and pharmacokinetic properties of the synthesized molecules[a]

Molecule	logS @ pH 7.4	logP	$logD_{7.4}$	MW	HBD	HBA	TPSA	Rotatable bonds
1	3.796	2.838	−0.13	398.4	3	9	141.3	6
4	−0.06904	3.587	3.587	426.4	2	9	130.3	8
5	0.3461	2.339	2.339	397.4	3	9	147.1	6
7	4.745	1.948	−1.41	321.3	3	8	142.4	4
11	3.697	2.678	−0.8747	257.2	3	5	86.63	4
12	3.541	2.927	−0.4391	285.3	3	5	86.63	6
14	3.557	3.533	0.7908	328.3	2	6	99.32	3
15	3.485	3.449	0.8726	328.3	2	6	99.32	3
18	2.447	1.506	1.506	279.3	1	7	104.9	4
19	2.252	2.624	2.624	278.3	1	6	91.99	4

Abbreviations: HBD, H-bond donors; HBA, #H-bond acceptors; logP, Predicted partition coefficient; $logD_{7.4}$, distribution coefficient at pH 7.4; MW, molecular weight in daltons; TPSA, topological polar surface area ($Å^2$); Rotatable Bond, # Rotatable bonds.
[a]logS @ pH 7.4: Predicted aqueous solubility at pH 7.4, log S. S in mol dm^{-3}.

3.3 | Molecular docking studies and molecular dynamics simulations

The open-out conformation of xCT was used for the docking studies. Initial docking runs with the open-occluded and inward-occluded conformations did not yield reasonable binding poses (data not shown). Hence, we explored further docking runs with the open-out conformation. Trial runs with SSZ (**1**) yielded only one binding pose using XP mode of Glide (Figure 4a). The —COO^- group of **1** interacted with Arg396 via a salt-bridge and a strong H-bonding interaction with Thr56 (Figure 4A). In addition, the other end of **1** showed edge-to-face π–π stacking interaction with Tyr241. The sulphonamide —NH formed a H-bond with Asn390. The hydrophobic central portion was found to interact with the hydrophobic amino acid residues such as Leu389, Ile142, Ala245 and others. Previously, isoxazole hydrazide inhibitors were shown to interact with Arg135 (cation-π interaction), Tyr251 (H-bonding), Ile134 (hydrophobic), Tyr244 (hydrophobic), Ser330 (H-bonding), Thr56 (H-bonding), etc. (Matti et al., 2013). Overall, similar ligand-antiporter interactions were found in our docking analyses as reported previously.

Trial runs with **1** to optimize docking run settings were followed by similar runs with the designed analogs of **1** (Table 1). Figure 4 shows the binding mode of **15** (IC_{50} = 116.74 μM) in the ligand-binding pocket of xCT. Here, the —COOH group in **1** was substituted with —SO_3H group. In addition to dominant salt-bridge interactions with Arg396, the acidic functionality in **15** also formed strong electrostatic interactions with Arg135. Arg396 also exhibited cation–π interaction with the aromatic ring bearing —SO_3H group. The hydrophobic naphthyl ring formed several interactions with the hydrophobic residues in the ligand-binding pocket of the antiporter. Similarly, **12**, a secondary amide (IC_{50} = 138 μM), exhibited similar binding mode with salt-bridge interaction with Arg135 and cation–π interaction of the acid-bearing aromatic ring with Arg369 (Figure 4c). Table 1 lists the major ligand-binding pocket residues interacting with the ligands.

We have compared the secondary structures of the xCT-SSZ complex from the docked state and during the MD simulations. The DSSP algorithm (Kabsch & Sander, 1983) was used to monitor the evolution of secondary structures over the entire 600 ns trajectory. While there were some transient turn and bend content in the expected locations, there were no pronounced changes in the helical content (66%).

The RMSDs were calculated for the xCT chain (backbone atoms only), residues in the binding pocket and ligand from the 600 ns trajectory with reference to the docked complex. The moving averages of the rmsds were smooth with an interval of 30. The moving average for the protein backbone at 600 ns converged at ~4 Å whereas the active site residues RMSD was ~3.3 Å (Figure S2). In case of the ligand, the plot showed that the ligand diffused from the original binding site during the production phase with 2–12 Å minimum RMSD relative to a top-ranked docking pose. The movement of the ligand could be attributed to various interactions as discussed further below.

The volume of the ligand cavity diverged from the docked complex during the simulations (Figure S3). Some divergence from the initial conformation was not unexpected when going from the docked structure environment to aqueous solution in the simulations and provided that there were various conformational changes reported for membrane receptors upon binding of the substrate or ligand. The change in volume of the ligand/substrate cavity could be explained by the rotation of the aromatic cluster consisting of three tyrosines (Tyr 240, 241 and 244) and the water occupancy in the cavity. Figure 6 shows the average side-chain torsion (chi1) rotation during simulation wherein Tyr241 and Tyr244 flip to alternate conformations. These residues are localized near the lipid/water interface and affect the binding of the ligand in the pocket. Grid and water H-bond analyses using CPPTRAJ tool in AMBER suggested the location of internal waters near the two Arginines (135 and 396) and Ser330.

Details of key H-bonding interactions and contacts between **1** and binding site within the xCT over the course of the MD simulations are presented in the Supporting Information (Table S3). From the data, it was clear that the intramolecular H-bond between the 2-hydroxyl

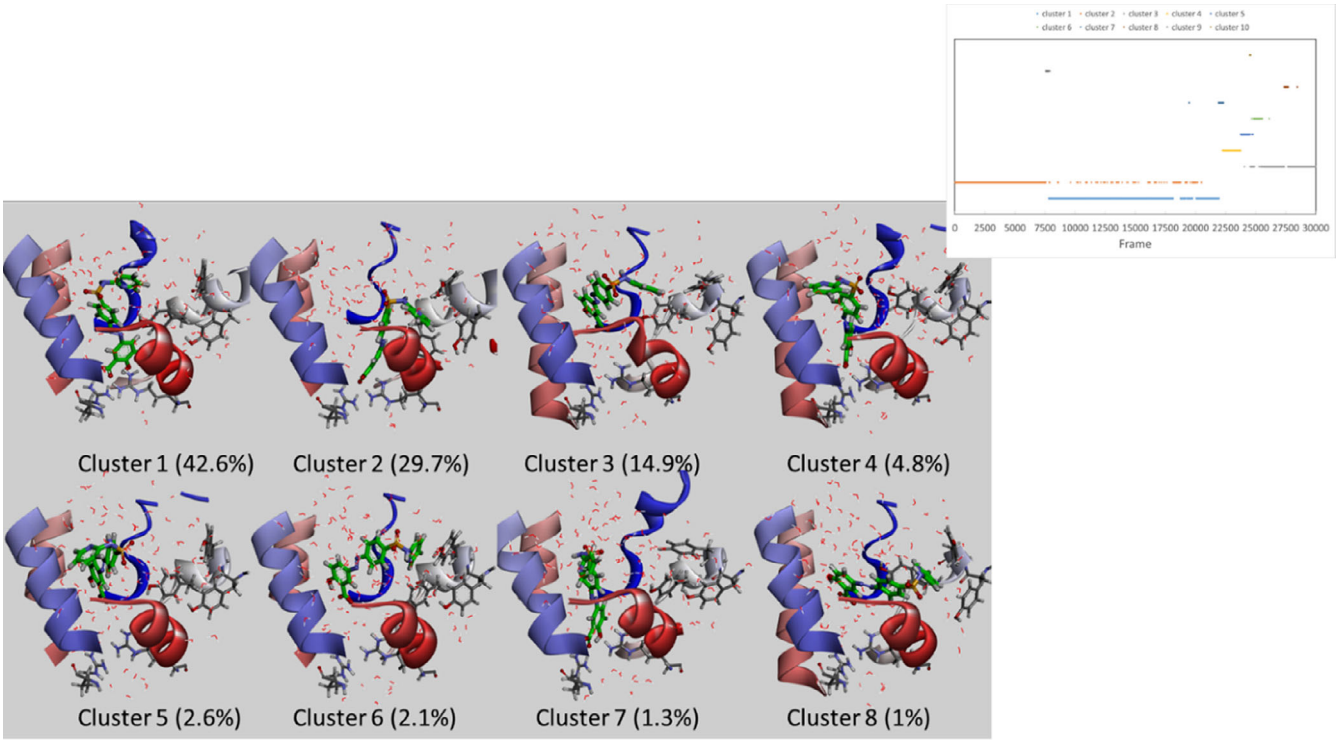

FIGURE 6 The conformation of ligand in the cavity obtained from clustering analysis on 30,000 frames based on the ligand fit. (frames were taken every 20 ps). The trajectory was divided into 10 clusters. Clusters 9 and 10 had <1% occupancy and therefore were not shown. Key residues Arg135, Arg396, Tyr240, Tyr241, and Tyr244 interacting with SSZ are shown for eight clusters. Water molecules are shown as lines, protein as ribbon colored from N (blue) to C-terminal (red) and residues as sticks. SSZ, sulfasalazine

group and the carbonyl O atom of the carboxylic acid group played a significant role in the stabilization of the molecule as highlighted in the monoclinic polymorphic crystal structure and quantum chemical studies (Patel & Gandhi, 2011). We believed this was one of the key features required for activity of SSZ analogs. The O atoms of the carboxylic acid moieties formed electrostatic interactions with the side chains of Arg135 and Arg136. Due to the conformational changes in the binding site, at around 500 ns, the carbonyl O atom of the —COOH group showed transient H-bonding with the side-chains of Ser330 or water-mediated H-bonds with Ser330, Arg135 and Arg136. Similar H-bonds were observed with the —COOH or its isosteric —SO_3H groups from ligands with either Arg135, Arg396 or both (Figure 4b,c).

Next, we performed RMSD-based structural clustering to identify distinct poses of the SSZ bound to the xCT. For SSZ, the clusters with occupancy >1% identified from the atomistic simulations are shown in Figure 6. The three most populated clusters reflected the ligand mobility with differences originating from interactions with residues in particular from helix-1 and helix-8. The interactions of the ligand with residues in the binding pocket are shown in Figure 7. The results indicated that in cluster 2, SSZ retains all native interactions with the protein as observed in the docked complex and at the start of the simulation. The carboxylic oxygens were involved in H-bonding with both arginines and the aromatic rings of SSZ were in close contacts with Tyr240, Tyr241, Tyr244, and Ala247 thus, forming π–π and π–alkyl interactions. The most populated cluster 1 showed reorientation of SSZ in the pocket. While the carboxylic group still retained interactions with the arginines in the active site, the native contacts with the aromatic triad of tyrosines were absent. Cluster 1 displayed role of π–sulfur interactions arising from the Cys327 residue of helix 8. This result indicated slight conformational changes were occurring upon ligand binding and was compatible with the previous study highlighting the role of Cys327 in substrate binding site (Jiménez-Vidal et al., 2004). Besides the top two clusters, other clusters showed transient interactions with the side chain of Ser330 and close contacts with Ile142 and Ala145.

A recent study based on the mutagenesis experiment and superposition of *C. glabrata* cystine transporter (Deshpande et al., 2017), CgCYN1 model onto mammalian cystine transporter xCT identified residues Cys327, Phe146, Ala247, Gly333, Leu389, and Val404 of *xCT* as critical for substrate binding. The SSZ-binding site in our model indicated an important role of Cys327, Ala247, Arg135, and 136, and other aromatic residues as discussed previously, whereas residues Phe146, Gly333, Leu389, and Val404 were within 5 Å from the SSZ-binding site. Our modeling reasonably was in agreement with their study on CgCYN1 despite <40% sequence similarity between the mammalian and yeast cystine transporter.

3.4 | In vitro Sx_c^- antiporter inhibition

A total of five series of title compounds were synthesized and tested for in vitro Sx_c^- inhibition. The potency data along with the molecular structures, docking scores, and interacting residues are given in Table 1. The Sx_c^- antiporter inhibition potential of the title

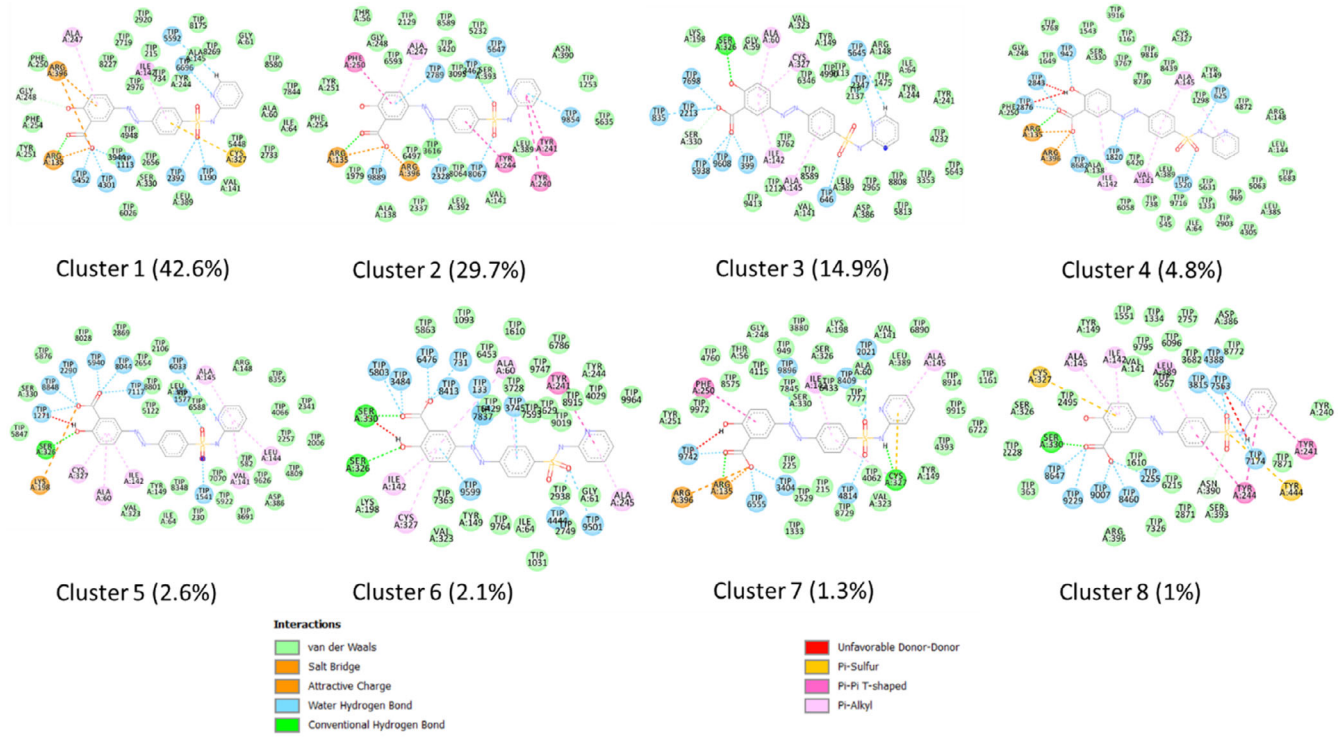

FIGURE 7 Details of various interactions of sulfasalazine with the receptor shown in a representative snapshot taken from the top eight clusters

compounds was evaluated using uptake assay in C6 glioma cell lines. A total of 13 out of 28 compounds were able to inhibit the antiporter activity in the IC_{50} range of 110–492 μM (Compound **1**, IC_{50} = 70 μM) (Table 1). These potency ranges (i.e., higher μM) are in accordance with the previous reports for **1** and its analogs (Matti et al., 2013; Shukla et al., 2011).

The structure–activity relationship (SAR) for Sx_c^- antiporter inhibition can be highlighted as follows: (a) conversion of **1** to its ester (**4**) led to improved cellular activity without much loss (~30%) in potency (76 μM vs 111 μM, Table 1). Masking one of the polar functionalities of **1** led to improved cellular activity, as expected. Further conversion of the ester to the amide (**5**) led to reduced in vitro potency. This could potentially be due to the neutral nature of the primary amide (—$CONH_2$ in **5**) compared to the highly acidic —COOH group, thereby compromising the salt-bridge interaction with either Arg135 or Arg396. 2) Removal of the terminal pyridine ring in **1** (compound **7**) resulted in complete loss of antiporter activity. This activity loss was surprising despite the presence of the proximal salicylic acid functionality. The absence of the pyridine ring might have compromised the anchoring of the molecule in the ligand-binding pocket, thereby potentially interfering with the favorable interactions between the ligands and the corresponding residues that mattered. Moreover, the removal of pyridine ring is likely to reduce $logD_{7.4}$ compared to **1** (Table 2). (c) Replacement of the azo linkage with the secondary amide (—CONH—) group along with the pyridine sulfonamido group completely abolished the antiporter activity (**11**, Table 1). Further extension of the —CONH— group by ethylene linker regained the potency, albeit less than **1** (**12**, Table 1). (d) In an attempt to identify suitable replacement for the salicylic acid moiety, α- and β-naphthol substructures were tried. To our surprise, one of the two compounds, **15** picked up the moderate activity (IC_{50} = 116 μM), compared to **14**, which was completely inactive (IC_{50} > 500 μM). As seen from the binding mode (Figure 4), **15** formed salt-bridge interactions between the highly acidic SO_3^- group and the two arginines (135 and 396). The presence of 2-OH group favorably led to H-bonding interaction with the backbone —C═O of Ile57. 5) Other modifications involving deletion of the azo linkage with simultaneous boisosteric replacement of the salicylic acid moiety with neutral –NO_2 group identified **18** with two-fold less potency compared to **1** (IC_{50} = 170 μM). Further replacing the pyridine heterocycle in **18** with the corresponding carbocycle (**19**) reduced potency further, delineating the important role of pyridine in biding of **1** with the antiporter. Overall, the study identified around five moderately potent (within two-fold potency on the lower side from **1**) inhibitors of Sx_c^-. The SAR was found to be realtively steep. This is in accordance with the earlier reports (Shukla et al., 2011).

3.5 | Sx_c^- inhibitors show anticancer potential in human glioblastoma cells

Because there could be potential differences between mouse (C6 cell line) and human glioblastoma cells in terms of sensitivity towards Sx_c^- inhibitors, we analyzed the anticancer activity of the five identified Sx_c^- inhibitors (hits) (**4**, **5**, **12**, **15** and **19**) along with **1** on the human glioblastoma cells (U87 MG and SF268) and compared it with their activity (potency) against C6 cell line. The cytotoxic activity was

determined by MTT assay. All the five inhibitors showed cytotoxicity for U87 cell lines with an IC_{50} range of 38.24–169.1 μM (Table 1). However, only two Sx_c^- inhibitors (**4** and **19**) were able to inhibit proliferation of SF268 cell line, albeit at quite high concentration. Being a highly malignant cell line, SF268 might express efflux transporters leading to lower effective cellular concentration. We could not understand this low potency by the hit molecules. The two glioma cell lines used although are both glioma grade IV but have different genetic background. These data suggest that compounds **4** and **19** are the most promising in terms of potentiating cell death of glioma cells irrespective of their genetic background. Since C6 cell line was used for the primary screening, we evaluated all the hits in MTT assay using C6 cell line. Compound **5** was the most potent hit with IC50 48.71 ± 6.9 μM while **4** was a close competitor (IC50 = 53.04 ± 6.2 μM). On the similar lines, **19** was slightly (1.five-fold) less potent than **1**.

4 | CONCLUSIONS

The present study culminated in high-quality homology model of system x_c^- antiporter based on AdiC and ApcT as the high-resolution templates. The 12 transmembrane all-helical models clearly showed the hydrophobic substrate-binding site lined by TM2, TM6, TM8 and TM10. Of the three models, the outward-open was the best choice for molecular docking studies. SSZ, a well-known Sx_c^- inhibitors was used for optimizing docking run settings followed by molecular dynamics simulations for 600 ns. The results clearly indicates the contribution of various residues in the ligand binding pocket for crucial interactions with the ligands. The intramolecular H-bond of the salicylic acid moiety was found crucial for overall binding and resultant antiporter inhibition. The proposed and validated binding mode is likely to help in guiding further design of potential Sx_c- inhibitors. The in vitro and cellular assays identified moderately potent hits 4 and 19 as potential antiporter inhibitors. Though 4 is likely to act as prodrug of 1, it reassured that acid functionality was not critical requirement. This has greater implication in terms of BBB penetration for glioblastoma treatment since acids are likely to be prevented from entering in brain.

ACKNOWLEDGMENTS

MN thank Department of Biotechnology (DBT), Neurobiology Task Force (NTF) for supporting the present work as a Research Grant to MN (Reference No. BT/PR4605/MED/30/719/2012). MN, DP and PK thank SVKM's NMIMS (Deemed to be University) for providing all the necessary facilities for smooth conduct of the presented work.

CONFLICT OF INTEREST

The authors declare that they have no potential conflict of interest.

ORCID

Mukesh Nandave https://orcid.org/0000-0002-6535-6505

REFERENCES

Abraham, M. J., Murtola, T., Schulz, R., Páll, S., Smith, J. C., Hess, B., & Lindahl, E. (2015). GROMACS: High performance molecular simulations through multi-level parallelism from laptops to supercomputers. *SoftwareX*, *1-2*, 19–25. https://doi.org/10.1016/j.softx.2015.06.001

Balendiran, G. K., Dabur, R., & Fraser, D. (2004). The role of glutathione in cancer. *Cell Biochemistry and Function*, *22*(6), 343–352. https://doi.org/10.1002/cbf.1149

Case, D. A., Walker, R. C., Thomas, E. C., 3rd, Simmerling, C., Roitberg, A., Kenneth, M. M., … Betz, R. (2016). *Amber 16*. San Francisco, CA: University of California.

Cassetta, L., & Pollard, J. W. (2018). Targeting macrophages: Therapeutic approaches in cancer. *Nature Reviews Drug Discovery*, *17*, 887–904. https://doi.org/10.1038/nrd.2018.169

Chen, D., Fan, Z., Rauh, M., Buchfelder, M., Eyupoglu, I. Y., & Savaskan, N. (2017). ATF4 promotes angiogenesis and neuronal cell death and confers ferroptosis in a xCT-dependent manner. *Oncogene*, *36*(40), 5593–5608. https://doi.org/10.1038/onc.2017.146

Chen, D., Rauh, M., Buchfelder, M., Eyupoglu, I. Y., & Savaskan, N. (2017). The oxido-metabolic driver ATF4 enhances temozolamide chemoresistance in human gliomas. *Oncotarget*, *8*(31), 51164–51176. https://doi.org/10.18632/oncotarget.17737

Chintala, S., Tóth, K., Yin, M. B., Bhattacharya, A., Smith, S. B., Ola, M. S., … Rustum, Y. M. (2010). Downregulation of cystine transporter xc by irinotecan in human head and neck cancer FaDu xenografts. *Chemotherapy*, *56*(3), 223–233. https://doi.org/10.1159/000316334

Clemons, N. J., Liu, D. S., Duong, C. P., & Phillips, W. A. (2017). Inhibiting system xC- and glutathione biosynthesis - a potential Achilles' heel in mutant-p53 cancers. *Molecular & Cellular Oncology*, *4*(5), e1344757. https://doi.org/10.1080/23723556.2017.1344757

Čolović, M., Rousseau, E., Zhang, Z., Lau, J., Zhang, C., Kuo, H. T., … Lin, K. S. (2018). Synthesis and evaluation of an ^{18}F-labeled boramino acid analog of aminosuberic acid for PET imaging of the antiporter system x_C. *Bioorganic & Medicinal Chemistry Letters*, *28*(22), 3579–3584. https://doi.org/10.1016/j.bmcl.2018.06.014

Dahlmanns, M., Yakubov, E., Chen, D., Sehm, T., Rauh, M., Savaskan, N., & Wrosch, J. K. (2017). Chemotherapeutic xCT inhibitors sorafenib and erastin unraveled with the synaptic optogenetic function analysis tool. *Cell Death Discovery*, *3*, 17030. https://doi.org/10.1038/cddiscovery.2017.30

Davis, I. W., Leaver-Fay, A., Chen, V. B., Block, J. N., Kapral, G. J., Wang, X., … Richardson, D. C. (2007). MolProbity: All-atom contacts and structure validation for proteins and nucleic acids. *Nucleic Acids Research*, *35*(Web Server issue), 375–383. https://doi.org/10.1093/nar/gkm216

Deshpande, A. A., Sharma, M., & Bachhawat, A. K. (2017). Insights into the molecular basis for substrate binding and specificity of the fungal cystine transporter CgCYN1. *Biochimica et Biophysica Acta (BBA) – Biomembranes*, *1859*(11), 2259–2268.

Dixon, S. J., Patel, D. N., Welsch, M., Skouta, R., Lee, E. D., Hayano, M., … Stockwell, B. R. (2014). Pharmacological inhibition of cystine-glutamate exchange induces endoplasmic reticulum stress and ferroptosis. *eLife*, *3*, e02523. https://doi.org/10.7554/eLife.02523

Dundas, J., Ouyang, Z., Tseng, J., Binkowski, A., Turpaz, Y., & Liang, J. (2006). CASTp: Computed atlas of surface topography of proteins with structural and topographical mapping of functionally annotated residues. *Nucleic Acids Research*, *34*(Web Server), W116–W118. https://doi.org/10.1093/nar/gkl282

Durrant, J. D., Votapka, L., Sørensen, J., & Amaro, R. E. (2014). POVME 2.0: An enhanced tool for determining pocket shape and volume characteristics. *Journal of Chemical Theory and Computation*, *10*(11), 5047–5056. https://doi.org/10.1021/ct500381c

Essmann, U., Perera, L., Berkowitz, M. L., Darden, T., Lee, H., & Pesersen, L. G. (1995). A smooth particle mesh Ewald method. *Journal*

of Chemical Physics, *103*, 8577–8593. https://doi.org/10.1063/1.470117

Fotiadis, D., Kanai, Y., & Palacin, M. (2013). The SLC3 and SLC7 families of amino acid transporters. *Molecular Aspects of Medicine*, *34*(2–3), 139–158. https://doi.org/10.1016/-j.mam.2012.10.007

Friesner, R. A., Banks, J. L., Murphy, R. B., Halgren, T. A., Klicic, J. J., Mainz, D. T., … Shenkin, P. S. (2004). Glide: A new approach for rapid, accurate docking and scoring. 1. Method and assessment of docking accuracy. *Journal of Medicinal Chemistry*, *47*, 1739–1749. https://doi.org/10.1021/jm0306430

Friesner, R. A., Murphy, R. B., Repasky, M. P., Frye, L. L., Greenwood, J. R., Halgren, T. A., … Mainz, D. T. (2006). Extra precision glide: Docking and scoring incorporating a model of hydrophobic enclosure for protein−ligand complexes. *Journal of Medicinal Chemistry*, *49*(21), 6177–6196. https://doi.org/10.1021/jm051256o

Gao, X., Zhou, L., Jiao, X., Lu, F., Yan, C., Zeng, X., … Shi, Y. (2010). Mechanism of substrate recognition and transport by an amino acid antiporter. *Nature*, *463*(7282), 828–832. https://doi.org/10.1038/nature08741

Granito, A., Marinelli, S., Negrini, G., Menetti, S., Benevento, F., & Bolondi, L. (2016). Prognostic significance of adverse events in patients with hepatocellular carcinoma treated with sorafenib. *Therapeutic Advances in Gastroenterology*, *9*(2), 240–249. https://doi.org/10.1177/-1756283X15618129

Guan, J., Lo, M., Dockery, P., Mahon, S., Karp, C. M., Buckley, A. R., … Wang, Y. Z. (2009). The xc- cystine/glutamate antiporter as a potential therapeutic target for small-cell lung cancer: Use of sulfasalazine. *Cancer Chemotherapy and Pharmacology*, *64*(3), 463–472. https://doi.org/10.1007/s00280-008-0894-4

Habib, E., Linher-Melville, K., Lin, H. X., & Singh, G. (2015). Expression of xCT and activity of system xc(−) are regulated by NRF2 in human breast cancer cells in response to oxidative stress. *Redox Biology*, *5*, 33–42. https://doi.org/10.1016/j.redox.2015.03.003

Halgren, T. A., Murphy, R. B., Friesner, R. A., Beard, H. S., Frye, L. L., … Banks, J. L. (2004). Glide: A new approach for rapid, accurate docking and scoring. 2. Enrichment factors in database screening. *Journal of Medicinal Chemistry*, *47*(7), 1750–1759. https://doi.org/10.1021/jm030644s

Hess, B., Bekker, H., Herman, J. C. B., & Johannes, G. E. M. F. (1997). LINCS: A linear constraint solver for molecular simulations. *Journal of Computational Chemistry* 1997, *18*(12), 1463–1472. https://doi.org/10.1002/(SICI)1096-987X(199709)18:12<1463::AID-JCC4>3.0.CO;2-H

Hoover, W. G. (1985). Canonical dynamics: Equilibrium phase-space distributions. *Physical Review A*, *31*(3), 1695–1697. https://doi.org/10.1103/PhysRevA.31.1695

Ishimoto, T., Nagano, O., Yae, T., Tamada, M., Motohara, T., Oshima, H., … Saya, H. (2011). CD44 variant regulates redox status in cancer cells by stabilizing the xCT subunit of system xc(−) and thereby promotes tumor growth. *Cancer Cell*, *19*(3), 387–400. https://doi.org/10.1016/j.ccr.2011.01.038

Jacobson, M. P., Friesner, R. A., Xiang, Z., & Honig, B. (2002). On the role of the crystal environment in determining protein side-chain conformations. *Journal of Molecular Biology*, *320*(3), 597–608. https://doi.org/10.1016/S0022-2836(02)00470-9

Jacobson, M. P., Pincus, D. L., Rapp, C. S., Day, T. J. F., Honig, B., Shaw, D. E., & Friesner, R. A. (2004). A hierarchical approach to all-atom protein loop prediction. *Proteins*, *55*(2), 351–367. https://doi.org/10.1002/prot.10613

Jeschke, G. A. (2013). A comparative study of structures and structural transitions of secondary transporters with the LeuT fold. *European Biophysical Journal*, *42*(2–3), 181–197. https://doi.org/10.1007/s00249-012-0802-z

Jiménez-Vidal, M., Gasol, E., Zorzano, A., Nunes, V., Palacín, M., & Chillarón, J. (2004). Thiol modification of cysteine 327 in the eighth transmembrane domain of the light subunit xCT of the heteromeric cystine/glutamate antiporter suggests close proximity to the substrate binding site/permeation pathway. *Journal of Biological Chemistry*, *279*(12), 11214–11221. https://doi.org/10.1074/jbc.M309866200

Jo, S., Kim, T., & Im, W. (2007). Automated builder and database of protein/ membrane complexes for molecular dynamics simulations. *PLoS One*, *2*(9), e880. https://doi.org/10.1371/journal.pone.0000880

Kabsch, W., & Sander, C. (1983). Dictionary of protein secondary structure: Pattern recognition of hydrogen-bonded and geometrical features. *Biopolymers*, *22*(12), 2577–2637. https://doi.org/10.1002/bip.360221211

Kharkar, P. S. (2014). Drugs acting on central nervous system (CNS) targets as leads for non-CNS targets. *F1000Research*, *3*, 40. https://doi.org/10.12688/f1000research.3-40.v2

Kharkar, P. S. (2017). Cancer stem cell (CSC) inhibitors: A review of recent patents (2012-2015). *Expert Opinion on Therapeutic Patents*, *27*(7), 753–761. https://doi.org/10.1080/13543776.2017.1325465

Kowalczyk, L., Ratera, M., Paladino, A., Bartoccioni, P., Errasti-Murugarren, E., Valencia, E., … Palacín, M. (2011). Molecular basis of substrate-induced permeation by an amino acid antiporter. *Proceedings of the National Academy of Sciences of the United States of America*, *108*(10), 3935–3940. https://doi.org/10.1073/pnas.1018081108

Krivov, G. G., Shapovalov, M. V., & Dunbrack, R. L., Jr. (2009). Improved prediction of protein side-chain conformations with SCWRL4. *Proteins*, *77*(4), 778–795. https://doi.org/10.1002/prot.22488

Lee, J., Cheng, X., Swails, J. M., Yeom, M. S., Eastman, P. K., Lemkul, J. A., … Im, W. (2016). CHARMM-GUI input generator for NAMD, GROMACS, AMBER, OpenMM, and CHARMM/OpenMM simulations using the CHARMM36 additive force field. *Journal of Chemical Theory and Computation*, *12*(1), 405–413. https://doi.org/10.1021/acs.jctc.5b00935

Liu, D. S., Duong, C. P., Haupt, S., Montgomery, K. G., House, C. M., Azar, W. J., … Clemons, N. J. (2017). Inhibiting the system xC−/glutathione axis selectively targets cancers with mutant-p53 accumulation. *Nature Communications*, *8*, 14844. https://doi.org/10.1038/ncomms14844

Liu, X., Rush, T., Zapata, J., & Lobner, D. (2009). Beta-N-methylamino-l-alanine induces oxidative stress and glutamate release through action on system xc(−). *Experimental Neurology*, *217*(2), 429–433. https://doi.org/10.1016/j.expneurol.2009.04.002

Lo, M., Ling, V., Wang, Y. W., & Gout, P. W. (2008). The x_c^- cystine/-glutamate antiporter: A mediator of pancreatic cancer growth with a role in drug resistance. *British Journal of Cancer*, *99*(3), 464–472. https://doi.org/10.1038/sj.bjc.6604485

Matti, A. A., Mirzaei, J., Rudolph, J., Smith, S. A., Newell, J. L., Patel, S. A., … Natale, N. R. (2013). Microwave accelerated synthesis of isoxazole hydrazide inhibitors of the system xc- transporter: Initial homology model. *Bioorganic Medicinal Chemistry*, *23*(21), 5931–5935. https://doi.org/10.1016/j.bmcl.2013.08.080

McCormick, P. N., Greenwood, H. E., Glaser, M., Maddocks, O. D. K., Gendron, T., Sander, K., … Witney, T. H. (2019). Assessment of tumor redox status through (S)-4-(3-[^{18}F]fluoropropyl)-L-glutamic acid positron emission tomography imaging of system xc- activity. *Cancer Research*, *79*(4), 853–863. https://doi.org/10.1158/0008-5472.CAN-18-2634

Miladinovic, T., Ungard, R. G., Linher-Melville, K., Popovic, S., & Singh, G. (2018). Functional effects of TrkA inhibition on system xC--mediated glutamate release and cancer-induced bone pain. *Molecular Pain*, *14*, 1744806918776467. https://doi.org/10.1177/1744806918776467

Nosé, S. (1984). A molecular dynamics method for simulations in the canonical ensemble. *Molecular Physics*, *52*(2), 255–268. https://doi.org/10.1080/00268978400101201

Nosé, S., & Klein, M. N. (1983). Constant pressure molecular dynamics for molecular systems. *Molecular Physics*, *50*(5), 1055–1076. https://doi.org/10.1080/002689-78300102851

Okuno, S., Sato, H., Kuriyama-Matsumura, K., Tamba, M., Wang, H., Sohda, S., … Bannai, S. (2003). Role of cystine transport in intracellular glutathione level and cisplatin resistance in human ovarian cancer cell lines. *British Journal of Cancer*, *88*(6), 951–956. https://doi.org/10.1038/sj.bjc.6600786

Palacín, M., Errasti-Murugarren, E., & Rosell, A. (2016). Heteromeric amino acid transporters. In search of the molecular bases of transport cycle mechanisms. *Biochemical Society Transactions*, *44*(3), 745–752. https://doi.org/10.1042/BST20150294

Parrinello, M., & Rahman, A. (1981). Polymorphic transitions in single crystals: A new molecular dynamics method. *Journal of Applied Physics*, *52*, 7182–7190. https://doi.org/10.1063/1.328693

Patel, D., Kharkar, P. S., & Nandave, M. (2015). Emerging roles of system Xc- antiporter and its inhibition in CNS disorders. *Molecular Membrane Biology*, *32*(4), 89–116. https://doi.org/10.3109/-09687688.2015.1096972

Patel, S. A., Rajale, T., O'Brien, E., Burkhart, D. J., Nelson, J. K., Twamley, B., … Natale, N. R. (2010). Isoxazole analogues bind the system xc- transporter: Structure-activity relationship and pharmacophore model. *Bioorganic & Medicinal Chemistry*, *18*(1), 202–213. https://doi.org/10.1016/j.bmc.2009.11.001

Patel, U., & Gandhi, S. A. (2011). Quantum chemical studies on crystal structures of sulphacetamide and sulphasalazine. *Indian Journal of Pure & Applied Physics*, *49*(4), 263–269.

Pettersen, E. F., Goddard, T. D., Huang, C. C., Couch, G. S., Greenblatt, D. M., Meng, E. C., & Ferrin, T. E. (2004). UCSF chimera--a visualization system for exploratory research and analysis. *Journal of Computational Chemistry* 2004, *25*, 1605–1612. https://doi.org/10.1002/jcc.20084

Robe, P. A., Martin, D. H., Nguyen-Khac, M. T., Artesi, M., Deprez, M., Albert, A., … Bours, V. (2009). Early termination of ISRCTN45828668, a phase 1/2 prospective, randomized study of sulfasalazine for the treatment of progressing malignant gliomas in adults. *BMC Cancer*, *9*, 372. https://doi.org/10.1186/1471-2407-9-372

Salas-Vega, S., Iliopoulos, O., & Mossialos, E. (2017). Assessment of overall survival, quality of life, and safety benefits associated with new cancer medicines. *JAMA Oncology*, *3*(3), 382–390. https://doi.org/10.1001/jamaoncol.2016.4166

Sali, A., & Blundell, T. L. (1993). Comparative protein modelling by satisfaction of spatial restraints. *Journal of Molecular Biology*, *234*(3), 779–815. https://doi.org/10.1006/jmbi.1993.1626

Sastry, G. M., Adzhigirey, M., Day, T., Annabhimoju, R., & Sherman, W. (2013). Protein and ligand preparation: Parameters, protocols, and influence on virtual screening enrichments. *Journal of Computer-Aided Molecular Design*, *27*, 221–234. https://doi.org/10.1007/s10822-013-9644-8

Sato, H., Tamba, M., Ishii, T., & Bannai, S. (1999). Cloning and expression of a plasma membrane cystine/glutamate exchange transporter composed of two distinct proteins. *Journal of Biological Chemistry*, *274*, 11455–11458. https://doi.org/10.1074/jbc.274.17.11455

Sato, M., Kusumi, R., Hamashima, S., Kobayashi, S., Sasaki, S., Komiyama, Y., … Sato, H. (2018). The ferroptosis inducer erastin irreversibly inhibits system xc- and synergizes with cisplatin to increase cisplatin's cytotoxicity in cancer cells. *Scientific Reports*, *8*(1), 968.

Schrödinger Suite 2015-4. (2015). *Protein Preparation Wizard; Epik version 3.4; Impact version 6.9; Prime version 4.2*. Schrödinger, LLC, New York, NY.

Sehm, T., Fan, Z., Ghoochani, A., Rauh, M., Engelhorn, T., Minakaki, G., … Savaskan, N. (2016). Sulfasalazine impacts on ferroptotic cell death and alleviates the tumor microenvironment and glioma-induced brain edema. *Oncotarget*, *7*(24), 36021–36033. https://doi.org/10.18632/oncotarget.8651

Shaffer, P. L., Goehring, A., Shankaranarayanan, A., & Gouaux, E. (2009). Structure and mechanism of a Na+–independent amino acid transporter. *Science*, *325*(5943), 1010–1014. https://doi.org/10.1126/science.1176088

Shah, C. P., & Kharkar, P. S. (2018). Discovery of novel human inosine 5′-monophosphate dehydrogenase 2 (hIMPDH2) inhibitors as potential anticancer agents. *European Journal of Medicinal Chemistry*, *158*, 286–301. https://doi.org/10.1016/j.ejmech.2018.09.016

Shukla, K., Thomas, A. G., Ferraris, D. V., Hin, N., Sattler, R., Alt, J., … Tsukamoto, T. (2011). Inhibition of x_c^- transporter-mediated cystine uptake by sulfasalazine analogs. *Bioorganic & Medicinal Chemistry Letters*, *21*(20), 6184–6187. https://doi.org/10.1016/j.bmcl.-2011.07.081

Söding, J. (2005). Protein homology detection by HMM-HMM comparison. *Bioinformatics*, *21*(7), 951–960. https://doi.org/10.1093/bioinformatics/bti125

Söding, J., Biegert, A., & Lupas, A. N. (2005). The HHpred interactive server for protein homology detection and structure prediction. *Nucleic Acids Research*, *33*(Web Server), W244–W248. https://doi.org/10.1093/nar/gki408

Sontheimer, H. (2008). A role for glutamate in growth and invasion of primary brain tumors. *Journal of Neurochemistry*, *105*(2), 287–295. https://doi.org/10.1111/j.1471-4159.2008.05301.x

Sosa, V., Moliné, T., Somoza, R., Paciucci, R., Kondoh, H., & LLeonart, M. E. (2013). Oxidative stress and cancer: An overview. *Ageing Research Reviews*, *12*(1), 376–390. https://doi.org/10.1016/j.arr.2012.10.004

van de Loosdrecht, A. A., Beelen, R. H., Ossenkoppele, G. J., Broekhoven, M. G., & Langenhuijsen, M. M. (1994). A tetrazolium-based colorimetric MTT assay to quantitate human monocyte mediated cytotoxicity against leukemic cells from cell lines and patients with acute myeloid leukemia. *Journal of Immunological Methods*, *174*(1–2), 311–320.

Verrey, F., Clossm, E. I., Wagner, C. A., Palacin, M., Endou, H., & Kanai, Y. (2004). CATs and HATs: The SLC7 family of amino acid transporters. *Pflugers Archiv: European Journal of Physiology*, *447*(5), 532–542. https://doi.org/10.1007/s00424-003-1086-z

Wagner, C. A., Lang, F., & Bröer, S. (2001). Function and structure of heterodimeric amino acid transporters. *American Journal of Physiology. Cell Physiology*, *281*(4), C1077–C1093. https://doi.org/10.1152/ajpcell.2001.281.4.C1077

Wang, X. Y., Li, Y. L., Wang, H. Y., Zhu, M., Guo, D., Wang, G. L., … Chen, Y. M. (2017). Propofol inhibits invasion and proliferation of C6 glioma cells by regulating the Ca^{2+} permeable AMPA receptor-system x_c^- pathway. *Toxicology in Vitro*, *44*, 57–65. https://doi.org/10.1016/j.tiv.2017.06.026

Wu, E. L., Cheng, X., Jo, S., Rui, H., Song, K. C., Dávila-Contreras, E. M., … Im, W. (2014). CHARMM-GUI membrane builder toward realistic biological membrane simulations. *Journal of Computational Chemistry*, *35*(27), 1997–2004. https://doi.org/10.1002/-jcc.23702

Wu, S., & Zhang, Y. (2007). LOMETS: A local meta-threading-server for protein structure prediction. *Nucleic Acids Research*, *35*(10), 3375–3382. https://doi.org/10.1093/nar/gkm251

SUPPORTING INFORMATION

Additional supporting information may be found online in the Supporting Information section at the end of this article.

How to cite this article: Patel D, Kharkar PS, Gandhi NS, Kaur E, Dutt S, Nandave M. Novel analogs of sulfasalazine as system x_c^- antiporter inhibitors: Insights from the molecular modeling studies. *Drug Dev Res*. 2019;1–20. https://doi.org/10.1002/ddr.21557